

Horizontal distribution of tropospheric NO₂ and aerosols derived by dual-scan multi-wavelength MAX-DOAS measurements in Uccle, Belgium

5 Ermioni Dimitropoulou¹, François Hendrick¹, Martina M. Friedrich¹, Frederik Tack¹, Gaia Pinardi¹, Alexis Merlaud¹, Caroline Fayt¹, Christian Hermans¹, Frans Fierens² and Michel Van Roozendael¹

¹ Royal Belgian Institute for Space Aeronomy (BIRA-IASB), Brussels, 1180, Belgium

² IRCEL-CELINE, Brussels, Belgium

Correspondence to: Ermioni Dimitropoulou (ermioni.dimitropoulou@aeronomie.be)

Abstract

10 Dual-scan ground-based Multi-AXis Differential Optical Absorption Spectroscopy (MAX-DOAS) measurements of tropospheric nitrogen dioxide (NO₂) and aerosols were carried out in Uccle (50.8°N, 4.35°E; Brussels region, Belgium) for two years, from March 2018 to February 2020. The MAX-DOAS instrument was operating in both UV and Visible wavelength ranges in a dual-scan configuration consisting of two sub-modes: (1) an elevation scan in a fixed viewing azimuthal direction and (2) an azimuthal scan in a fixed low elevation angle (2°). By analyzing the O₄ and NO₂ dSCDs at six different wavelength
15 intervals along every azimuthal direction and by applying a new Optimal-Estimation-based inversion approach (the so-called mapping MAX-DOAS technique), the horizontal distribution of the NO₂ near-surface concentrations and vertical column densities (VCDs) and the aerosols near-surface extinction coefficient are retrieved along ten azimuthal directions. The retrieved horizontal NO₂ concentration profiles allow the identification of the main NO₂ hotspots in the Brussels area. Correlative comparisons of the retrieved horizontal NO₂ distribution were conducted with airborne, mobile, air-quality model, and satellite
20 datasets, and overall a good agreement is found. The comparison with TROPOMI observations, from operational and scientific data products, reveals that the characterization of the horizontal distribution of tropospheric NO₂ VCDs by ground-based measurements, ~~the appropriate sampling of TROPOMI pixels~~, and an adequate a priori NO₂ profile shape in TROPOMI retrievals lead to a better consistency between satellite and ground-based datasets.

1 Introduction

25 Aerosols and nitrogen dioxide (NO₂) play a crucial role in the tropospheric chemistry. NO₂ is an important tropospheric pollutant mainly emitted by combustion processes and nitrogen fertilizers used in agriculture (Seinfeld and Pandis, 1998). Traffic, domestic heating, industrial activities, and power plants are the largest NO₂ emitters (Tack et al., 2021). Beyond its harmful effects on human health (Chen et al., 2007), NO₂ participates in the formation of tropospheric ozone (O₃) by a non-linear photochemical mechanism which involves volatile organic compounds (VOCs).

30 Aerosols with a small diameter can penetrate deeply into the lungs, causing millions of premature deaths around the world per year (Khomenko et al., 2021). Additionally, aerosols influence the Earth's climate system by changing its radiation budget by scattering and absorbing sunlight (Quaas et al., 2008). In the boundary layer of urban regions, the horizontal distribution of NO₂ is highly heterogeneous given the fact that it is a short-lived species (Beirle et al., 2003). For those reasons, the regional and global monitoring of NO₂ and aerosols at high spatial resolution is crucial.

35 Since 1995, with the ERS-2 GOME (Global Ozone Monitoring Experiment) instrument (Burrows et al., 1999), satellite nadir air-quality measurements of atmospheric backscattered sunlight in the UV-visible range have provided daily global tropospheric column measurements of numerous trace gases, such as NO₂. Many satellite missions dedicated to air-quality monitoring followed over the next years with increasing spatial resolution. More recently, the TROPospheric Monitoring Instrument (TROPOMI) sensor launched onboard the Sentinel-5P Precursor (S5P) platform in October 2017 reached an initial

40 spatial resolution of 7x3.5 km², and augmented on 6 August 2019 to 5.5x3.5 km². Due to TROPOMI's fine spatial resolution, monitoring the horizontal distribution of NO₂ in urban regions and identifying specific emission sources is made easier than with previous satellite missions but still, TROPOMI cannot fully capture the fine-scale (sub-kilometer) structures in the effective NO₂ field. Consequently, TROPOMI requires further attention concerning its measurements validation.

Tropospheric vertical columns of many trace gases like NO₂, formaldehyde (HCHO), sulphur dioxide (SO₂), nitrous acid

45 (HONO) and O₃ can be retrieved by the Multi-AXis Differential Optical Absorption Spectroscopy (MAX-DOAS) technique (Hönninger et al., 2004; Wittrock et al., 2004; Pinardi et al., 2008, 2013; Clémer et al., 2010; Hendrick et al., 2014; Irie et al., 2011, 2012; Sinreich et al., 2007; Wagner et al., 2011; Wang et al., 2018). In recent years, MAX-DOAS measurements have been widely used as reference datasets for the validation of nadir airborne and space-borne air-quality measurements. MAX-DOAS instruments measure the scattered sunlight in the UV and Visible spectral ranges at multiple elevation angles above the

50 horizon. For absorbers located close to the surface, such as tropospheric NO₂, the higher sensitivity is achieved for low MAX-DOAS elevation angles. During the last years, MAX-DOAS measurements in more than one azimuthal direction are emerging (Ortega et al., 2016; Wang et al., 2014; Chan et al., 2020; Schreier et al., 2021). Multi-azimuthal MAX-DOAS measurements offer many possibilities on air-quality monitoring, such as a better characterization of the effective NO₂ field around the station. These ground-based datasets can be valuable for validating satellite missions with fine spatial resolution in regions where the

55 NO₂ horizontal distribution is heterogeneous, such as urban and sub-urban areas.

In this study, a new aerosol and NO₂ horizontal distribution inversion approach based on two years (March 2018-February 2020) of dual-scan multi-wavelength MAX-DOAS measurements in Uccle (Brussels-Capital region, Belgium) is presented. We refer to this new approach as mapping MAX-DOAS technique. In every azimuthal viewing direction, parameterized NO₂ near-surface concentrations, NO₂ tropospheric columns and aerosol extinctions measured at six different wavelengths are used

60 as input in a new horizontal distribution inversion approach. On this basis, the near-surface aerosol extinction and NO₂ horizontal distributions are retrieved at a spatial resolution of about 3km in a range of about 20 km around the measurement site. These horizontal profiles are used to validate collocated TROPOMI tropospheric NO₂ columns. We use here (i) the operational TROPOMI data product, (ii) a so-called diagnostic data set, which is a small sample but with major updates

compared to the operational product (van Geffen et al., 2021b) and (ii) a European TROPOMI product where profiles from
65 CAMS regional CTM ensemble (S5P-CAMS) are used (Douros et al., 2021). One complete year of data (March 2018-March
2019) and two wavelength intervals (one in the UV and one in the Visible) have already been used in Dimitropoulou et al.
(2020). It is proven that multi-azimuthal (the so-called dual-scan) MAX-DOAS measurements significantly improve the
agreement between ground-based and TROPOMI tropospheric NO₂ column observations over the Brussels' area. By adding
the multi-wavelength aspect, the present work represents an extension of the former study.

70 The manuscript is organized into ~~six~~seven sections: in Sect. 2, the measurement site with the MAX-DOAS experimental set-
up and the multi-wavelength DOAS analysis are presented. In Sect. 3 ~~and~~ 4, the TROPOMI tropospheric NO₂ measurements
~~and ancillary measurements used in this study~~ are described, ~~respectively~~. Section 4~~5~~ is composed of two main parts: Sect.
4~~5~~.1 is a detailed description of the dual-scan multi-wavelength MAX-DOAS retrieval method and Sect. 4~~5~~.2 is the horizontal
aerosol and NO₂ distribution inversion approach (i.e., the mapping MAX-DOAS technique). In Sect. 5~~6~~, main results followed
75 by correlative comparisons of the retrieved ground-based and satellite horizontal NO₂ distribution are presented. Finally, in
Sect. 6~~7~~, conclusions and future perspectives are given.

2 Dual-scan multi-wavelength MAX-DOAS measurements

2.1 Measurement site and experiment set-up

Brussels-Capital Region is the most densely populated area in Belgium, where pollutant concentrations, such as NO₂, are often
80 high because of anthropogenic activities (Tack et al., 2021).

A MAX-DOAS dual-scan instrument was operated by BIRA-IASB (Koninklijk Belgisch Instituut voor Ruimte-Aeronomie –
Institut Royal d'Aeronomie Spatiale de Belgique) in Uccle from January 2017 to February 2020. Uccle is located to the South
of the city-center of Brussels and to the West of a large forested area (Bois de la Cambre). Therefore, it is an ideal site to
perform MAX-DOAS observations under moderate to high pollution level conditions. Additionally, the characterization of the
85 horizontal distribution of NO₂ and aerosols at high spatial resolution is of great interest here because of the heterogeneity of
the pollution sources (car traffic, national airport, power plant) in the capital region of Brussels.

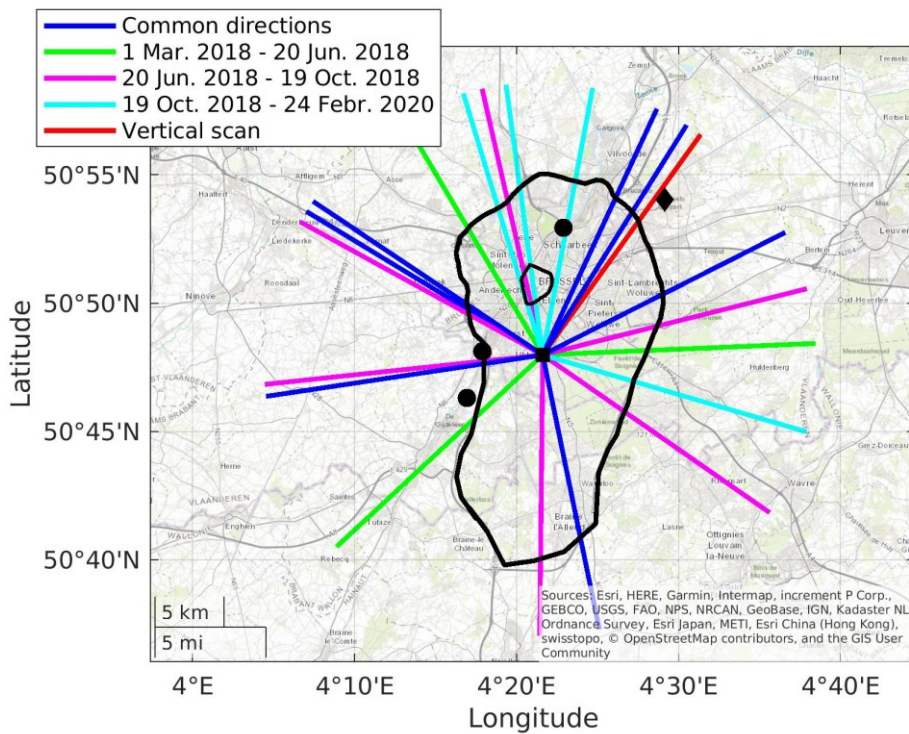
The MAX-DOAS dual-scan instrument is composed of the following parts: the optical head mounted on a sun tracker, two
spectrometers (UV and Visible) inside a thermo-regulated box and the data-acquisition unit. The optical head and the two
spectrometers are connected with optical fibers. A more detailed description of the BIRA-IASB MAX-DOAS dual-scan
90 instrument can be found in Dimitropoulou et al. (2020).

From March 2018 to February 2020, the MAX-DOAS instrument operated in a dual-scan viewing mode. Two different sub-
modes compose one complete measurement scan (see Dimitropoulou et al., 2020): (1) a vertical scan in nine different elevation
angles (EAs) in one fixed telescope azimuth angle (TAA; Northeast direction i.e., towards the city center and the national
airport) and (2) a horizontal scan in nine different azimuthal directions at a fixed elevation angle (2° above the horizon).

95 Several azimuthal viewing directions were tested to obtain an optimal horizontal sampling without any obstacle in the different viewing directions (see Fig. 1). The selection of more azimuthal directions towards the North, Northeast, and Northwest was made considering the location of the main NO₂ emission sources and, consequently, the highly variable NO₂ horizontal distribution towards these directions.

The integration time for each measured radiance spectrum is 60s, resulting in a full scan duration of approximately 20 minutes.

100



105 **Figure 1.** The experimental set-up of the BIRA-IASB dual-scan MAX-DOAS instrument. Each line is color-coded according to the different set-ups that were used from March 2018 to February 2020. The length of each line is equal to 20 km, which corresponds to the typical horizontal sensitivity for the MAX-DOAS measurements in the present

study (see Fig. 18). The black square shows the MAX-DOAS instrument location, the black polygon the National Airport, the black dots the NO₂ hotspots emitting more than 10 kg of NO_x per hour (Emission Inventory of the Belgian Interregional Environment Agency, 2017) , and the black line represents the Brussels Ring motorway.

2.2 Multi-wavelength DOAS analysis

The measured radiance spectra of a full measurement scan are analyzed using the QDOAS spectral fitting software developed by BIRA-IASB (Fayt et al., 2011). The DOAS technique separates the narrow absorption features of trace gases in the UV-Visible spectral range from a spectral background caused mainly by Mie and Rayleigh scattering and instrumental effects. The trace gas concentration integrated along the light-path in a measured spectrum relative to the amount of the same absorber in a reference spectrum is the primary product of the DOAS analysis and is called differential slant column density (dSCD). Here, average zenith spectra before and after each measurement scan are used as a reference.

The O₄ and NO₂ dSCDs are retrieved in six different wavelength intervals: Three intervals in the UV spectral range (330-361 nm, 350-370 nm, and 360-383.5 nm) and three in the Visible range (420-460 nm, 450-490 nm, and 510-540.1 nm). These fitting windows were selected to optimize the determination of the O₄ and NO₂ dSCDs at the maximum number of different O₄ absorption bands available in the wavelength domain of the instrument. Figure 2 shows an example of the O₄ and NO₂ fits in all the intervals used in the present work. In each chosen fitting window, we select a reference wavelength, which corresponds to the maximum of an O₄ absorption peak (or close to it) in the respective wavelength intervals (see Fig. 2), and it is subsequently used for radiative transport calculations and further analysis. The different reference wavelengths are 343 nm, 360 nm, 380 nm, 447 nm, 477 nm and 530 nm (see Fig. 2). To optimize the derivation of the dSCDs at the six selected wavelengths, the fit of a slope parameter, which accounts for the variation of the dSCD within the fitting interval (Puķīte et al., 2010), is necessary. This is especially important when the reference wavelength is not located in the center of the fitting window (i.e., 330-361 nm, 350-370 nm, 420-460 nm, and 450-490 nm). The DOAS settings used for each fitting interval are presented in Table S1. As shown in this table, two different O₄ cross-sections are used in this study: (1) Finkenzeller (private communication and Volkamer, (2022)) in the UV fitting intervals and (2) Thalman and Volkamer, (2013) in the Vis fitting intervals. The main motivation for using the O₄ cross-section from Finkenzeller (measured at 25°C) in the UV fitting intervals is the significant improvement of the fit quality and the reduction of the uncertainties for the UV retrievals. Sensitivity tests and comparisons with radiative transport simulations also show that the resulting O₄ and NO₂ dSCDs are consistent throughout the whole wavelength range covered by the six intervals. For NO₂ and O₃, which are the strongest absorbers in all the fitting windows, a correction for the solar I₀ effect (Aliwell et al., 2002) is applied. A high-resolution solar atlas (Kurucz et al., 1984) is used for the wavelength calibration of the measured spectra.

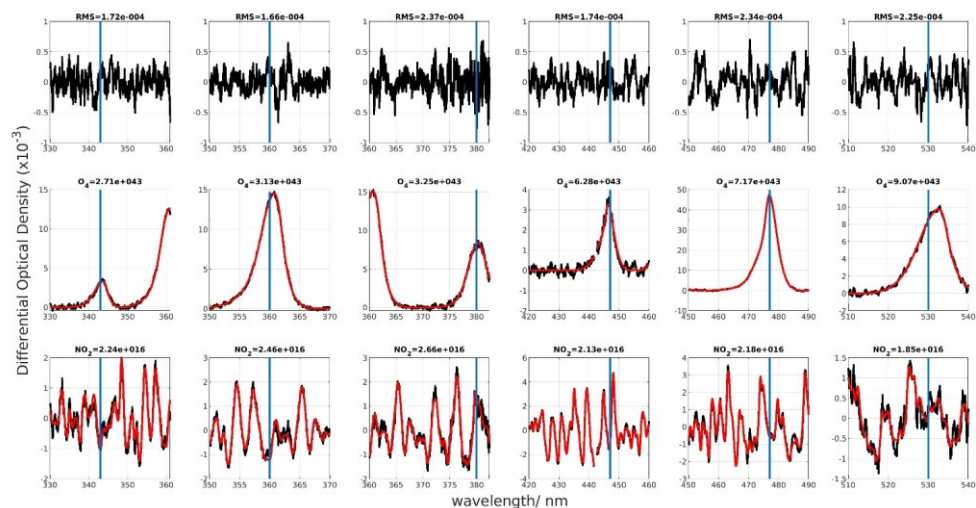


Figure 2. Fit results of the O₄ and NO₂ fit at the six selected fitting windows from the dual-scan MAX-DOAS measurements in Uccle (2 June 2019 at 07:05 UTC). The measured spectra are represented with black lines, while the fit results are shown with red lines. The blue lines represent the six reference wavelengths.

3 TROPOMI tropospheric NO₂ measurements

In the present study, MAX-DOAS tropospheric NO₂ VCDs are used to validate collocated TROPOMI satellite observations. TROPOMI is a passive grating imaging spectrometer flying onboard the S5P satellite platform. It covers the UV-Visible (250-500 nm), near-infrared (710-770 nm), and short-wave infrared (2314-2382 nm) spectral ranges (Veeffkind et al., 2011). TROPOMI measures in a push-broom configuration with a full swath width as wide as 2600 km, and it provides daily global coverage at a spatial resolution (true-nadir pixel size) of 7x3.5 km², further improved to 5.5x3.5 km² on 6 August 2019. The TROPOMI tropospheric NO₂ algorithm has been developed at KNMI and uses a retrieval-assimilation-modeling system that is based on the 3-D global TM5 chemistry transport model (van Geffen et al., 2021a; Williams et al., 2017).

We use the reprocessed (RPRO) and offline (OFFL) datasets of the TROPOMI L2 tropospheric NO₂ column product (see Table 1 for the corresponding versions). According to the guidelines provided by van Geffen et al. (2021a), RPRO dataset are available only for the first period of the present study (see Table 1). For the remaining periods, OFFL datasets are used, which are the main data products being available within two weeks from the TROPOMI measurement. To ensure best measurements'

quality, only pixels with a quality assurance value larger than 0.75 are used. This quality flagging eliminates pixels with a cloud radiance fraction larger than 0.5, snow or ice, and erroneous retrievals (Eskes and Eichmann, 2020).

160 Next to operational products, two additional TROPOMI data sets are also used (see Section S2 in the supplement). In the first one, the TROPOMI retrieval is performed with different a priori profiles (Douros et al., in preparation). The coarse TM5-MP a priori NO₂ profiles, using a spatial resolution of 1° x 1°, is replaced by NO₂ profile shapes from the CAMS (Copernicus Atmospheric Monitoring Service) regional Chemistry Transport Model (CTM) ensemble at a spatial resolution of 0.1° x 0.1° (S5P-CAMS product). The replacement of a coarse a priori information by a finer one can lead to significant changes in the
165 TROPOMI retrieved NO₂ tropospheric columns. The available dataset covers October 2018 to March 2020 (OFFL dataset, L2, and version 01.02.00 up to 01.04.00, Eskes and Eichmann, 2020).

In the second additional product, the TROPOMI retrieval is performed with an improved cloud product (Eskes et al., 2020; van Geffen et al., 2021a). According to van Geffen et al. (2021a), the improvement in the FRESCO-S cloud pressure retrieval scheme to the FRESCO-wide product, has an impact on the NO₂ AMFs and consequently, on the NO₂ tropospheric columns
170 over polluted areas. More precisely, the existing FRESCO-S product had a negative bias in the cloud height values, which resulted in a low NO₂ tropospheric column (Compernelle et al., 2021). The TROPOMI tropospheric NO₂ columns are retrieved using an improved FRESCO-S cloud retrieval scheme, called FRESCO-wide, in v1.4 since 29 November 2020 (Eskes and Eichmann, 2020). In the present study, the diagnostic data sets (DDSv2) are used, which are an ensemble of reprocessed data for past periods analyzed with new versions (van Geffen et al., 2021b). Over the MAX-DOAS measurement time-period, only
175 DDSv2 data corresponding to OFFL datasets (v1.2 and v1.3) are available. Excluding the spin-up period needed by TM5-MP, only four data periods are available for our comparisons (i.e., 30/06/2018 - 06/07/2018, 30/12/2018 - 5/01/2019, 30/03/2019-05/04/2019, and 17/09/2019-23/09/2019).

Table 1. TROPOMI NO₂ processor versions used in the present study.

Dataset	Version	Starting date	End date
RPRO	01.02.02	30/04/2018	17/10/2018
OFFL	01.02.00	17/10/2018	28/11/2018
OFFL	01.02.02	28/11/2018	20/03/2019
OFFL	01.03.00	20/03/2019	23/04/2019
OFFL	01.03.01	23/04/2019	26/06/2019
OFFL	01.03.02	26/06/2019	29/11/2020

180

4 Ancillary measurements

In the present study, ancillary measurements are used for two main purposes: (1) as a priori information on the retrieval of the MAX-DOAS NO₂ and aerosol horizontal profiles and (2) to validate the retrieved MAX-DOAS NO₂ horizontal profiles.

185 First, the CIMEL Sun photometer is a multi-channel photometer, which measured the direct solar irradiance and sky radiance at the Earth's surface in discrete wavelengths in the UV, Visible and near-IR wavelengths of the spectrum. Aerosol optical thickness measurements at the Brussels-Capital Region from a co-located CIMEL Sun photometer of the AERONET network (<https://aeronet.gsfc.nasa.gov/>) are used on the retrieval of the MAX-DOAS aerosol horizontal profiles (see Section 5.3).

190 Secondly, independent NO₂ horizontal profile, used as a priori information in the new OEM-based horizontal distribution inversion approach, are provided by the RIO model. RIO is a land-use regression model based on the interpolation of the hourly NO₂ near-surface concentrations measured by the in-situ telemetric air quality network in Belgium (Hooyberghs et al., 42006; Janssen et al., 2008; see <http://irceline.be/en>). RIO provides hourly NO₂ concentration maps on a 4x4 km² spatial resolution.

To validate the retrieved MAX-DOAS NO₂ horizontal profiles, independent measurements are necessary in the Brussels-Capital Region.

195 For the SSP validation campaign over Belgium (SSPVAL-BE, <https://s5pcampaigns.aeronomie.be/>), airborne measurements of the two largest urban regions over Belgium, i.e., Antwerp and Brussels, took place from 26 to 29 June 2019 (Tack et al., 2021). The Airborne Prism EXperiment (APEX) imaging spectrometer was used to measure the horizontal distribution of tropospheric NO₂ columns with a spatial resolution of approximately 75 m x 120 m (Tack et al., 2017; Tack et al., 2019). During the SSPVAL-BE flight over Brussels, car mobile-DOAS observations were performed by the BIRA-IASB mobile-DOAS, the so-called AEROMOBIL (Merlaud, 2013). The AEROMOBIL consists of a compact double Avantes spectrometer recording simultaneously scattered light in two elevation angles (i.e., one at 30° elevation angle and one at zenith). The AEROMOBIL was used to measure the spatial distribution of tropospheric NO₂ columns mainly over the Ring road of Brussels. These airborne and car-mobile measurements are compared with the retrieved MAX-DOAS NO₂ horizontal profiles (see Section 6.2).

205 5 Description of the mapping MAX-DOAS technique

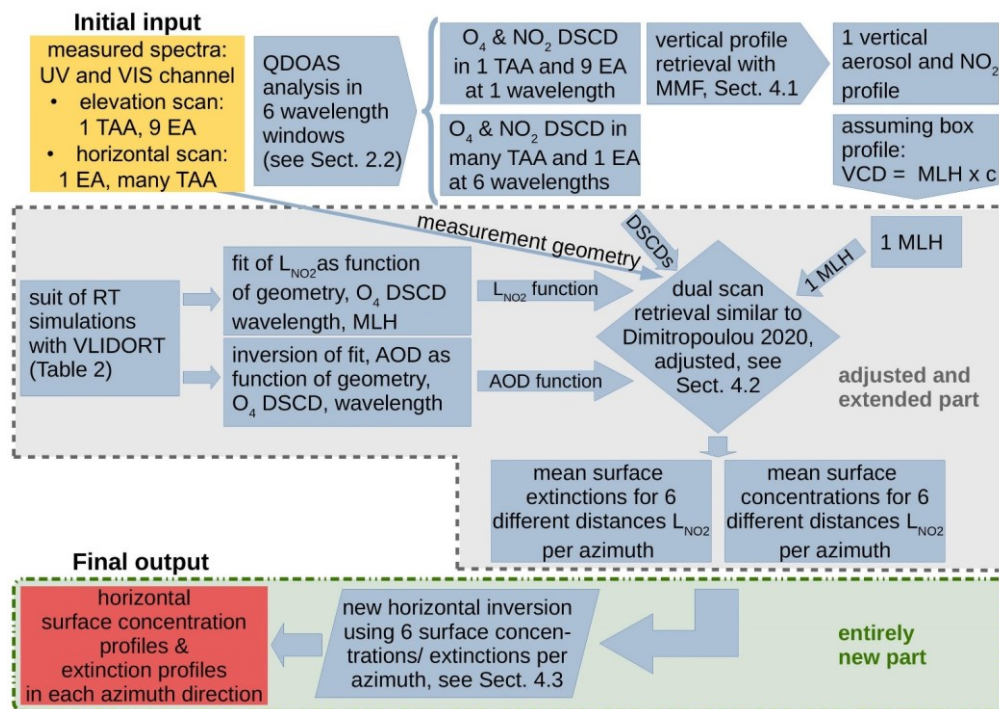
First, the measured radiance spectra in the UV and Visible wavelength ranges are analyzed in the six different fitting windows with the main output being the O₄ and NO₂ dSCDs at six wavelengths, which are 343 nm, 360 nm, 380 nm, 447 nm, 477 nm and 530 nm (see listed in Section 2.2). Then, the Optimal Estimation Method (OEM)-based Mexican MAX-DOAS Fit (MMF) algorithm is applied to the O₄ and NO₂ dSCDs in the main azimuthal direction (and at 477 nm) to retrieve vertical NO₂ profiles and obtain information about the vertical extent of NO₂ in the troposphere via the Mixing Layer Height of NO₂ (MLH_{NO₂}; see Section 4.5.1).

As an intermediate step, radiative transfer model (RTM) simulations are performed (see Table 2 and Section 4.5.2) to obtain information about the horizontal sensitivity (L_{NO_2}) and AOD as a function of O_4 dSCDs, wavelength, and MLH_{NO_2} .

Then, in the next step, a new dual-scan parameterization technique is applied to the O_4 and NO_2 dSCDs at the six different wavelengths and in all the azimuthal directions with MLH_{NO_2} , measured O_4 dSCDs, and measurement geometry being the main input parameters to retrieve the horizontal sensitivity of NO_2 and, consequently, the NO_2 near-surface concentrations and VCDs, and near-surface aerosol extinction as a function of distance from the instrument (see Section 4.5.2).

In the final step, a new OEM-based horizontal distribution inversion approach is developed using the six near-surface NO_2 concentrations and aerosol extinction values per azimuthal direction to retrieve horizontal NO_2 and aerosol extinction horizontal profiles in an output horizontal grid of 500m thickness (see Section 4.5.3).

A flow chart describing the mapping MAX-DOAS technique is shown in Fig. 3.



225 Figure 3. Mapping MAX-DOAS technique flow chart.

4.5.1 Aerosol and NO₂ OEM-based profile retrievals

The Optimal-estimation-based ~~Mexican~~ MAX-DOAS Fit (MMF) inversion algorithm (Friedrich et al., 2019) is applied to retrieve the aerosol extinction coefficient and NO₂ vertical profiles for each MAX-DOAS elevation scan in the main azimuthal direction at 360 nm and 477 nm. First, the O₄ measurements are used to retrieve the aerosol extinction profile. Several studies indicated the importance of applying a scaling factor ($\neq 1$) to the observed O₄ dSCDs to bring them in agreement with simulated O₄ dSCDs by radiative transfer modeling (Wagner et al., 2009; Cl mer et al., 2010; Merlaud et al., 2011; see also Wagner et al., 2019 / Table 1 for a comprehensive list of all those studies). However, there is no consensus on the fundamental reason for applying this scaling (see e.g. Ortega et al., 2016). As found by Tirpitz et al. (2021), the choice of the scaling factor has only a small effect on the performance of the trace gas retrieval, so we decided not to apply it in the present study. The aerosol extinction profile retrieved from each scan is used as an input to the radiative transfer calculations used to retrieve the NO₂ retrieval profile. Further details about the MMF inversion algorithm, the input a priori parameters, the quality check of each scan, and the estimated uncertainties of the aerosol and NO₂ vertical profile can be found in Dimitropoulou et al. (2020).

A broken cloud-filtering approach based on Gielen et al. (2014) is applied to the MAX-DOAS measurements to exclude MAX-DOAS aerosol and NO₂ scans influenced by the presence of clouds, which are known to potentially degrade the quality of the retrievals (Gielen et al. 2014, Wagner et al. 2014). Three sky conditions can be distinguished with this flagging approach: (1) clear sky, (2) homogeneous cloud coverage and (3) broken clouds conditions. Retrievals under broken cloud conditions are rejected from the present study.

The profile retrieval was performed to estimate the Mixing Layer Height of NO₂ (MLH_{NO₂}). The MLH_{NO₂} is estimated per measurement scan, and it is the ratio of VCD_{NO₂,main} to the NO₂ near-surface concentration ($c_{\text{NO}_2,\text{main}}$) as retrieved in the main azimuthal direction by the MMF inversion algorithm:

$$\text{MLH}_{\text{NO}_2} = \frac{\text{VCD}_{\text{NO}_2,\text{main}}}{c_{\text{NO}_2,\text{main}}} \quad (1)$$

Therefore, during one measurement scan, two assumptions were made: (1) the homogeneous distribution of NO₂ inside the MLH_{NO₂} and (2) the homogeneous MLH_{NO₂} around the measurement site and its use in all the azimuthal directions. The validity of the second assumption is tested in Section 4.5.2.3.

4.5.2 Dual-scan MAX-DOAS retrieval method

A complete MAX-DOAS measurement scan is composed of two different sub-scans, as described in Sect. 2.1. The aerosol and NO₂ vertical profiles are retrieved from the elevation scan in the main azimuthal direction. In the other azimuthal directions, measurements are performed only in a single low elevation angle (2°), and therefore, the retrieval of aerosol and

NO₂ vertical profiles is not possible. Using the fact that the lowest elevation angles have the highest sensitivity to trace gases located nearby the surface due to the long light path in this layer, a new dual-scan MAX-DOAS retrieval strategy was developed here. This new retrieval strategy is an extension of the work presented in Dimitropoulou et al. (2020) and aims to retrieve the near-surface NO₂ box-averaged volume mixing ratios (VMRs) and the NO₂ VCDs at six different wavelengths. In Dimitropoulou et al. (2020), the applied dual-scan NO₂ MAX-DOAS retrieval was itself an adaptation of the parameterization technique proposed by Sinreich et al. (2013). More precisely, in the presence of sufficient aerosols in the atmosphere (i.e., sufficient aerosols to constrain the light path in a near-surface layer and ensure that the near-surface NO₂ concentration can be approximated by a near-surface box profile), the measured NO₂ dSCDs at one low elevation angle (2°) can be related to the near-surface NO₂ box-averaged concentration as follows:

$$dSCD_{NO_2} = c_{NO_2} L_{NO_2} \quad (2)$$

where $dSCD_{NO_2}$ is the differential slant column density of NO₂ and c_{NO_2} its mean concentration along the differential effective light path, L_{NO_2} .

Consequently, the knowledge of the differential effective light-path's length (i.e., L_{NO_2}) is crucial to derive the near-surface NO₂ concentrations. The oxygen collisional complex (O₄) can be used as a tracer for the effective light-path in the atmosphere, as its concentration is well-known (it is the square of O₂ concentration). As a result, observed changes of the O₄ dSCDs can be directly attributed to changes in the light-path due to the presence of particles like aerosols and clouds. L_{O_4} is calculated as follows: by using Eq. 2 for O₄.

$$L_{O_4} = \frac{dSCD_{O_4}}{c_{O_4}} \quad (3)$$

where c_{O_4} is the typical O₄ concentration at the altitude of the instrument.

However, the direct use of the O₄ light-path length in the NO₂ retrieval is not possible under moderate to high pollution conditions, such as those in Brussels, because the profile shapes of O₄ and NO₂ are not the same. In Dimitropoulou et al. (2020), we used radiative transfer model (RTM) simulations to estimate a unitless correction factor, which accounts for these profile shape differences. This unitless correction factor indicates that under moderate to high pollution conditions, L_{NO_2} is equal to or smaller than L_{O_4} . For a correction factor equal or close to one, L_{O_4} is equal to L_{NO_2} , which means that there is a moderate to high aerosol load in the atmosphere during the measurement. On the other hand, correction factors smaller than unity are obtained for measurements performed under aerosol-free conditions or a thin MLH. Assuming a homogeneous NO₂ distribution inside the MLH, the MLH is derived from the NO₂ vertical profiles in the main azimuthal direction and is defined as the ratio of the NO₂ VCD to the near-surface concentration of NO₂. In Dimitropoulou et al. (2020), the RTM simulations were performed for eight different MLH values of aerosols and NO₂ in the range of 500-2000 m (i.e. eight different

290 combinations) and for different measurement viewing geometries (Solar Zenith Angle (SZA), Relative Azimuth Angle (RAA) and the corresponding elevation angle of 2°). For every MAX-DOAS measurement, one value of the correction factor is given according to its viewing geometry and MLH value during the measurement. For further information, we refer the reader to Dimitropoulou et al. (2020).

In the present study, a new dual-scan NO₂ MAX-DOAS retrieval method, which is more suitable for interpreting multi-wavelength measurements than the previous approach (Dimitropoulou et al., 2020), is developed. It is presented in detail in the following subsection.

4.5.2.1 Developed dual-scan MAX-DOAS retrieval method

The main advantages of the new dual-scan NO₂ MAX-DOAS retrieval method (which are also the main differences with respect to Dimitropoulou et al., 2020) are the following: (1) the direct use of the measured O₄ dSCDs to estimate L_{NO₂} for every measurement, (2) retrieval of near-surface aerosol extinction close to the ground, and (3) the exploitation of the wavelength dependency of the horizontal path representative of MAX-DOAS measurements for the retrieval of the horizontal distribution of aerosols (and therefore NO₂) around the measurement site. The latter is done using O₄ and NO₂ dSCDs measured at six different wavelengths. This new method is described below.

Assuming that the NO₂ vertical distribution can be approximated by a box profile of height equal to mixing layer height (MLH_{NO₂}), the following equation can be used:

$$c_{NO_2} = \frac{VCD_{NO_2}}{MLH_{NO_2}} = \frac{dSCD_{NO_2}}{L_{NO_2}} \quad (43)$$

This means that the NO₂ near-surface concentration can be expressed as a ratio of the dSCD_{NO₂} to the L_{NO₂} (see Eq. 2) or as a ratio of the VCD_{NO₂} to the MLH_{NO₂}. When knowing MLH_{NO₂} and VCD_{NO₂}, L_{NO₂} can be simulated as follows:

$$L_{NO_2 \text{ simulated}} = dSCD_{NO_2 \text{ simulated}} \frac{MLH_{NO_2}}{VCD_{NO_2}} \quad (54)$$

Here, NO₂ dSCDs and consequently L_{NO₂} are simulated using the radiative transfer model VLIDORT version 2.7 (Spurr, 2006). Seasonal median MAX-DOAS NO₂ vertical profiles, as retrieved by applying the MMF inversion algorithm in the main azimuthal direction (see Sect. 4.5.1), show that the bulk (70 %) of the NO₂ concentration is located inside the MLH_{NO₂}, which is expected since MLH_{NO₂} is estimated as the ratio of VCD_{NO₂} to the near-surface NO₂ concentration. On the other hand, this is not the case for aerosols (only 30 % of the aerosol content is seen to be located inside the MLH_{NO₂}). Considering this feature, for the VLIDORT simulations, the NO₂ a priori profiles are modeled as box profiles with a constant concentration equal to 1.5x10¹¹ molec/cm³ from the surface to the MLH_{NO₂}. Two layers compose the aerosol a priori profiles: (1) the MLH_{NO₂} and

(2) the free troposphere. The equation, which is applied to estimate the aerosol extinction profile $a(z)$, is the following (see Wang et al., 2014):

$$a(z) = \text{AOD} \frac{p}{\text{MLH}_{\text{NO}_2}}, \text{ for } z \leq \text{MLH}_{\text{NO}_2} \quad (6a5a)$$

and,

$$a(z) = b(\xi, \text{MLH}_{\text{NO}_2}, p) \exp\left(-\frac{z}{\xi}\right), \text{ for } z > \text{MLH}_{\text{NO}_2} \quad (6b5b)$$

where AOD is the aerosol optical depth, p is the fraction of AOD inside the MLH_{NO_2} , b is a normalizing constant for the exponential component (Wang et al., 2014), z is the simulation altitude grid, and ξ is the scaling height for the aerosols located outside the MLH_{NO_2} , which is set to 5 km (Wang et al., 2014). In the present study, the fraction of AOD located within the MLH_{NO_2} is set to $p=0.3$ (see above). The effect of the p value and the NO_2 profile shape on the retrieved NO_2 near-surface VMRs and VCDs were investigated and considered in the error budget (see Sect. 4.5.2.2).

The MLH_{NO_2} is a known parameter and it is estimated per measurement scan, as the ratio of VCD_{NO_2} to the NO_2 near-surface concentration as retrieved in the main azimuthal direction by the MMF inversion algorithm.

The RTM simulations have in total nine input parameters, which are the elevation angle, SZA, RAA, AOD, MLH_{NO_2} , c_{NO_2} , AOD (p and ξ), and wavelength. It should be noted that the elevation angle is kept constant (i.e., 2°). For the six different wavelengths (343 nm, 360 nm, 380 nm, 447 nm, 477 nm, and 530 nm), we separately perform RTM simulations and L_{NO_2} (see Eq. 54) are simulated for the assumed SZA, RAA, MLH_{NO_2} , c_{NO_2} , and AOD input scenarios presented in Table 2.

Table 2. RTM inputs for the simulations of L_{NO_2} at the six selected wavelengths (343 nm, 360 nm, 380 nm, 447 nm, 477 nm, and 530 nm).

Parameter	Values
Wavelength/ nm	343, 360, 380, 447, 477, 530
SZA/ °	20, 30, 40, 50, 60, 70, 80
RAA/ °	0, 10, 20, 30, 40, 50, 60, 90, 120, 150, 180
AOD	0, 0.1, 0.3, 0.4, 0.6, 0.8, 1
p of AOD	0.30
ξ of AOD/ km	5
asymmetry parameter	0.68
Single Scattering Albedo (SSA)	0.92
MLH/ m	500, 1000, 1500
Elevation angle/ °	2

$$C_{\text{NO}_2} / \text{molec.cm}^{-3} \quad 1.5 \times 10^{11}$$

The simulated O_4 dSCDs are a function of the input parameter AOD. The relation between the simulated O_4 dSCDs and the input AOD values is shown in Fig. 4a. A Piecewise cubic hermite interpolating polynomial fitting through the AOD as a function of the simulated O_4 dSCDs for each SZA, RAA, and MLH_{NO_2} combination can be used in order to perform an inverse method (i.e. to estimate the near-surface aerosol extinction from the measured O_4 dSCDs). Additionally, in Fig.4b, we can see that the relation between the O_4 dSCDs and the AOD values is valid for MAX-DOAS measurements.

For every combination of all eight parameters (i.e., all the parameters of Table 2, except the AOD values), a polynomial fit of simulated L_{NO_2} as a function of simulated O_4 dSCDs is applied. Fig. 5a shows simulated L_{NO_2} as a function of simulated O_4 dSCDs, and a second-order polynomial is fitted through the data points. We observe, also, in Fig. 5b, in which an example day of MAX-DOAS measurements is presented, that the L_{NO_2} as a function of the measured O_4 dSCDs have the same relation as the simulated quantities. Since NO_2 is an optically thin absorber, L_{NO_2} is not a function of c_{NO_2} and consequently, a L_{NO_2} value can be estimated by using the measured O_4 dSCD for each measurement. Based on the corresponding SZA, RAA, measured O_4 dSCD, and MLH_{NO_2} , a L_{NO_2} is attributed to each low elevation MAX-DOAS measurement through this polynomial fit. To express L_{NO_2} as a function of four different parameters (i.e., O_4 dSCD, SZA, RAA, and MLH_{NO_2}), L_{NO_2} is interpolated linearly at the O_4 dSCD, SZA, RAA, and MLH_{NO_2} of each measurement. For example, a MAX-DOAS measurement with $\text{SZA}=30^\circ$, $\text{RAA}=60^\circ$, $\text{MLH}_{\text{NO}_2}=1\text{km}$, and measured O_4 dSCD= 6.10^{43} molec 2 .cm $^{-5}$ will have a L_{NO_2} equal to 15 km at 477 nm (see Fig. 5a).

Based on this approach, the near-surface NO_2 concentration can be calculated at the six different wavelengths by using the measured $\text{dSCD}_{\text{NO}_2}$ together with the simulated L_{NO_2} value (Eq. 2). The corresponding near-surface NO_2 VMR are obtained by dividing the NO_2 concentrations by the air number density. To derive the air number density, we use monthly averaged pressure and temperature profiles over a 20-year period. These profiles are extracted from the European Centre for Medium-Range Weather Forecasts (ECMWF) ERA-Interim reanalysis. In the last step, the tropospheric NO_2 VCD is calculated from the product of the near-surface NO_2 concentration with the MLH_{NO_2} .

Regarding the aerosols, the AOD is estimated for every off-axis measurement (see Fig. 4a). The near-surface aerosol extinction is then calculated as the ratio between the aerosols inside the MLH_{NO_2} (i.e., AOD times p) and MLH_{NO_2} . The near-surface aerosol extinction refers to the layer that extends from the surface to the MLH_{NO_2} . As mentioned above, around 30% of the total aerosols is expected to be found inside this layer.

The effect of SZA, RAA, and MLH_{NO_2} on the simulated L_{NO_2} is investigated in the supplement. First, the simulated L_{NO_2} are presented in Fig. S1 as a function of RAA for different MLH_{NO_2} and wavelengths and a single AOD and SZA value. L_{NO_2}

strongly depends on MLH_{NO_2} . The lower the MLH_{NO_2} , the shorter the L_{NO_2} is. The same NO_2 concentration and aerosol load are used for the three different MLH_{NO_2} scenarios. So, when aerosols are concentrated in a thin layer (i.e., $MLH_{NO_2}=0.5$ km), L_{NO_2} becomes shorter. Secondly, we observe that L_{NO_2} depends on RAA. The larger the RAA, the longer the L_{NO_2} . In Fig. S2, simulated L_{NO_2} are plotted for each wavelength and each considered MLH_{NO_2} as a function of SZA (at a constant AOD and RAA). L_{NO_2} depends strongly on SZA. The highest dependency is observed for large SZA values, where L_{NO_2} becomes maximum. Finally, in both Fig. S1 and S2, we observe that L_{NO_2} becomes longer with wavelength, which is expected because of the less pronounced Rayleigh and Mie scattering at longer wavelengths.

375

380

An example of dual-scan MAX-DOAS retrieval is shown in Fig. 6. Based on the RTM simulations described above, L_{NO_2} is derived for the wavelengths of interest, and ultimately, near-surface NO_2 concentrations and tropospheric NO_2 VCDs are estimated. In the last step, the near-surface aerosol extinction values are assigned to the six different wavelengths.

385

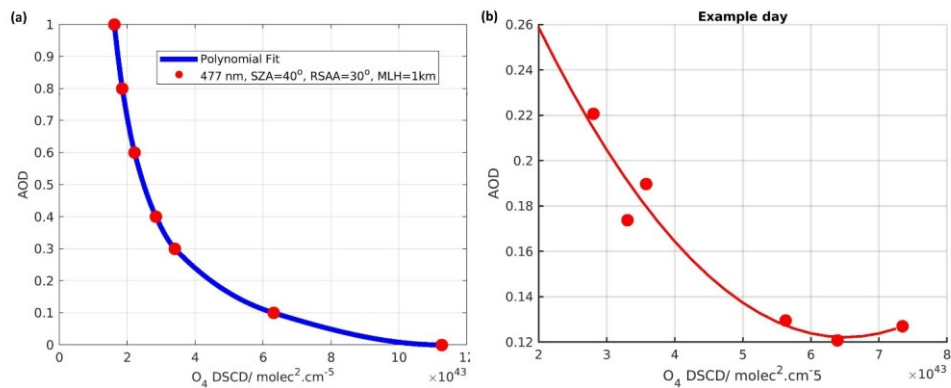


Figure 4. (a) Dots: Simulated AOD for NO_2 box profile of 1 km at 477nm for a SZA of 40° and RAA of 30° as a function of the simulated O_4 DSCDs for the different AOD values (1, 0.8, 0.6, 0.4, 0.3, 0.1 and 0; see Table 2). Blue line: simulated AOD by applying an exponential fit through the data points. (b) Dots: Estimated AOD in the six wavelengths used in the retrieval for one example day (11 September 2018). Red line: fitted line through the data points.

390

395

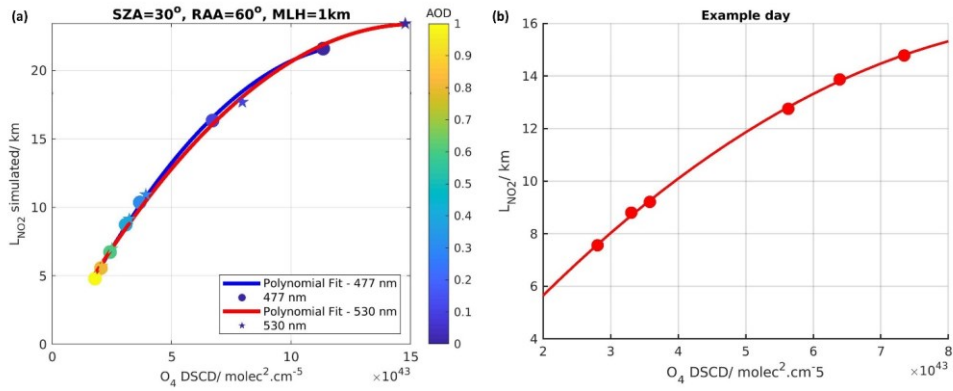
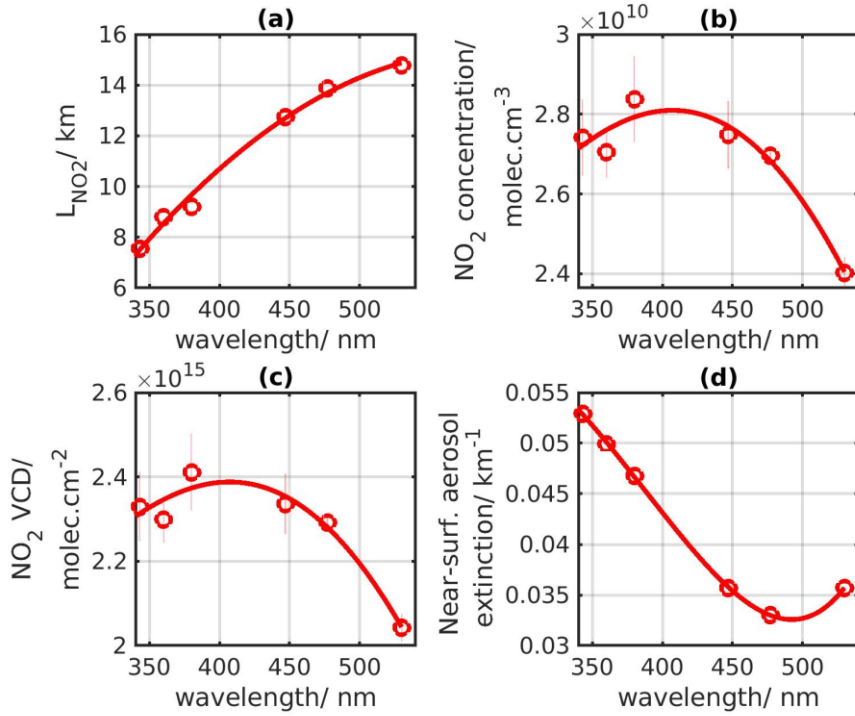


Figure 5. (a) Dots (stars): Simulated L_{NO_2} for NO_2 box profile of 1 km at 477nm (530 nm) for a SZA of 30° and RAA of 60° as a function of the simulated O_4 DSCDs for the different AOD values (1, 0.8, 0.6, 0.4, 0.3, 0.1 and 0; see Table 2). Blue (red) line: 2nd-order polynomial fit through the data points. (b) Dots: Estimated L_{NO_2} in the six wavelengths used in the retrieval for one example day (11 September 2018). Red line: fitted line through the data points.

400

405



410 **Figure 6. (a) Corresponding L_{NO_2} , (b) near-surface NO_2 concentrations, (c) NO_2 VCDs, and (d) aerosol optical densities as a function of the six wavelengths used in the retrieval (11 September 2018, 11:51 UTC, 123.5° azimuthal direction).**

45.2.2 Uncertainty budget

To estimate uncertainties on the dual-scan parameterized NO_2 near-surface concentration and VCD, the standard error propagation method is used as:

$$\sigma_{c_{NO_2}}^2 = \left(\sigma_{d_{SCD_{NO_2}}} \frac{\partial c_{NO_2}}{\partial d_{SCD_{NO_2}}} \right)^2 + \left(\sigma_{L_{NO_2}} \frac{\partial c_{NO_2}}{\partial L_{NO_2}} \right)^2 \quad (76)$$

which is solved as:

$$\sigma_{c_{NO_2}}^2 = \left(\frac{\sigma_{dSCD_{NO_2}}}{L_{NO_2}} \right)^2 + \left(-\frac{\sigma_{L_{NO_2}} dSCD_{NO_2}}{L_{NO_2}^2} \right)^2 \quad (87)$$

420

and then:

$$\sigma_{c_{NO_2}}^2 = \left(\sigma_{dSCD_{NO_2}} \frac{c_{NO_2}}{dSCD_{NO_2}} \right)^2 + \left(\sigma_{L_{NO_2}} \frac{c_{NO_2}}{L_{NO_2}} \right)^2 \quad (98)$$

where:

$$\sigma_{L_{NO_2}}^2 = \left(\frac{L_{NO_2}}{dSCD_{NO_2}(sim)} \sigma_{dSCD_{NO_2}} \right)^2 + \left(\frac{L_{NO_2}}{MLH_{NO_2}} \sigma_{MLH_{NO_2}} \right)^2 \quad (409)$$

425

According to Kreher et al. (2019) and Bösch et al. (2018), in urban or suburban polluted conditions, the use of the DOAS fit uncertainty of NO₂ for the dSCD_{NO₂} uncertainty is not appropriate, because the dSCD_{NO₂} uncertainty is mostly driven by atmospheric variability as well as spatial and temporal fluctuations in the O₄ and NO₂ fields. In this study, a conservative value of 3.5x10¹⁵ molec.cm⁻² is attributed to $\sigma_{dSCD_{NO_2}}$ (Kreher et al., 2019). This represents an error of up to 6.0% on the NO₂ dSCDs

430

in the visible range (477 nm).

The second error source is related to the estimation of L_{NO₂} from the RTM simulations. To estimate this error, sensitivity tests on the input aerosol and NO₂ vertical profiles were performed. The fraction of aerosols located inside the MLH_{NO₂} (40% and 60% instead of 30%) and the NO₂ profile shape (linearly decreasing instead of box) were modified. The error related to the RTM simulations of the simulated dSCD_{NO₂} is about 9.6% in the Visible range (477 nm). Additionally, according to

435

Dimitropoulou et al. (2020), the uncertainty related to MLH_{NO₂} is about 4% in the Visible range (477 nm).

Combining all the error sources, the total uncertainties on the NO₂ near-surface concentration is about 12.7%, 12.4%, 11.4%, 11.1%, 11.3%, and 12.6% in 343 nm, 360 nm, 380 nm, 447 nm, 477 nm, and 530 nm, respectively.

Finally, the total uncertainties on the NO₂ VCD is about 12.0%, 11.7%, 10.7%, 10.3%, 10.6%, and 11.9% in 343 nm, 360 nm, 380 nm, 447 nm, 477 nm, and 530 nm, respectively.

440

4.5.2.3 Verification of the dual-scan MAX-DOAS retrieval method

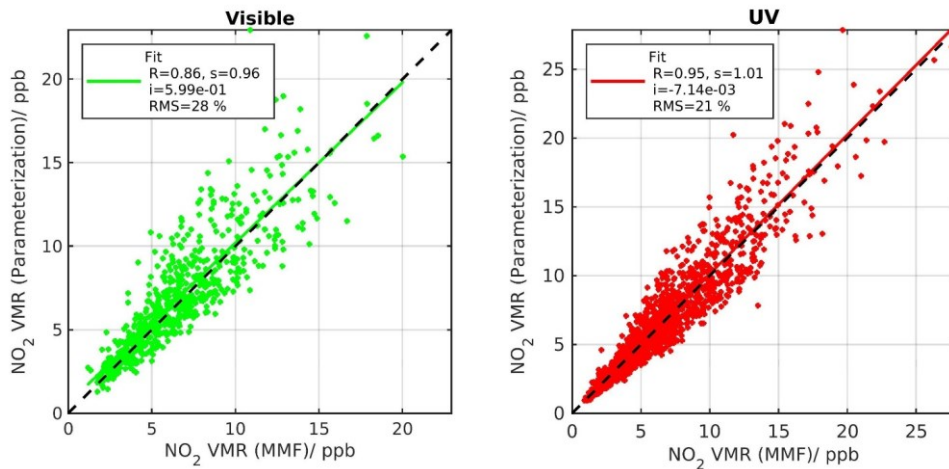
The [sanityconsistency](#) check and verification of the dual-scan MAX-DOAS retrieval method in Uccle is based on two different correlative comparisons.

445

The [sanityconsistency](#) check compares the NO₂ near-surface VMRs and tropospheric VCDs retrieved by the dual-scan parameterization in the main azimuthal direction to the same quantities retrieved with the MMF inversion algorithm at the two main wavelengths (360 nm and 477 nm). As can be seen in Figures 7 and 8, both data sets are in good agreement, with correlation coefficient values in the range of 0.86 to 0.95 and slope values close to unity for all the four comparisons.

450 The verification step is based on the same type of comparison as the first one but for three additional azimuthal directions, where elevation scans, and hence profile retrievals, are available for some periods. Onward July 3, 2019, elevation scans were performed in these three additional azimuthal directions to complement the already existing measurement set-up. These elevation scans were performed once per day, around noon, in the 11°, 105°, and 262.5° azimuthal directions. Figure 9 shows the comparison between near-surface NO₂ VMRs and tropospheric VCDs retrieved by the dual-scan parameterization method and the corresponding results obtained with the MMF inversion algorithm. Overall good agreement is obtained (R=0.79 and 0.84 for near-surface VMR and VCD, respectively). We observe that the comparison concerning the near-surface NO₂ VMR seems to be noisier than in the main azimuth direction. This is mainly due to the use of the MLH_{NO2} calculated in the main azimuthal direction for all the different azimuth angles in the dual-scan method. Additionally, the parameterization technique slightly underestimated the near-surface NO₂ VMR (s=0.84) while a slope value of 1.00 is obtained for tropospheric VCDs.

455



460 **Figure 7. Comparison between MMF and parameterized NO₂ near-surface VMR at 477 nm (Visible, left panel), and 360 nm (UV, right panel), as derived from the main azimuthal direction (i.e., 35.5° azimuthal direction).**

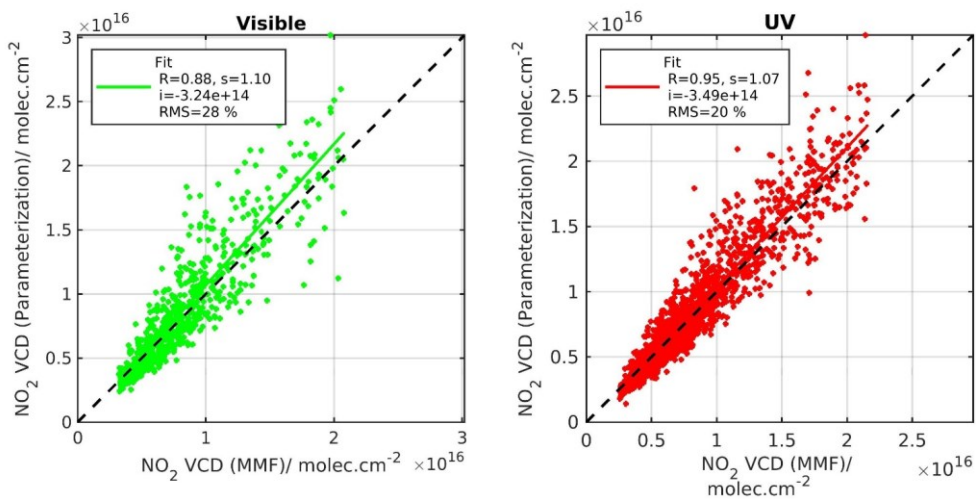


Figure 8. Comparison between MMF and parameterized NO₂ VCD at 477 nm (Visible, left panel), and 360 nm (UV, right panel), as derived from the main azimuthal direction (i.e., 35.5° azimuthal direction).
465

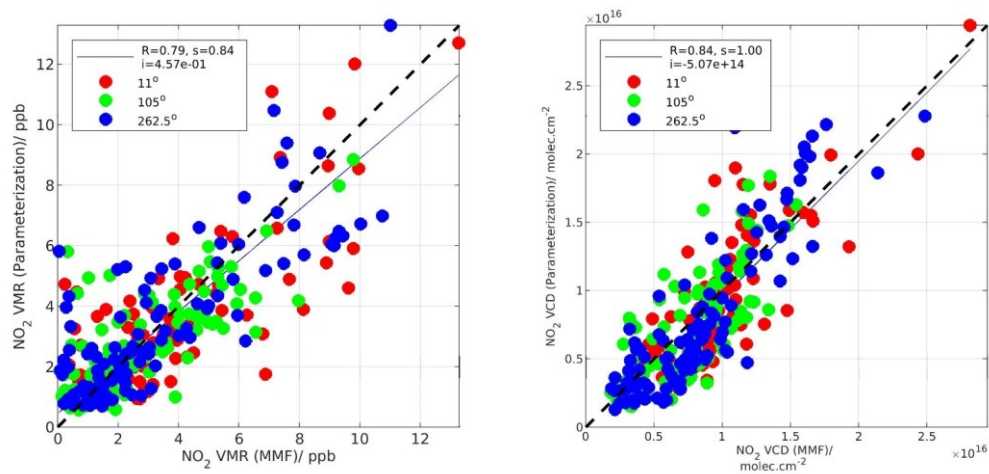


Figure 9. Visible range: comparison between MMF and (left panel) parameterized NO₂ near-surface VMR and (right panel) parameterized NO₂ VCD at three different azimuthal directions, as indicated in the color bar (11°, 105°, and 262.5° azimuthal directions). The elevation scans in these azimuthal directions were performed once per day from 3 July 2019.

4.5.3 Horizontal distribution inversion approach

The parameterized NO₂ near-surface concentrations at the six different wavelengths are used as input in a new horizontal distribution inversion approach. As parameterized NO₂ near-surface concentrations, we refer to the conversion of the measured NO₂ dSCDs (i.e. at the elevation angle of 2°) to near-surface NO₂ concentrations by applying the dual-scan MAX-DOAS retrieval method as described in Sect. 4.5.2. Figure 10 shows a sketch of the assumed horizontal box model configuration, in which successive boxes of concentration c_N between the horizontal distances $x_{\text{scd}_{N-1}}$ and x_{scd_N} from the MAX-DOAS instrument are considered along the light path. The index N is equal to the total number of successive boxes.

The different horizontal lines illustrate the horizontal extent (or differential effective light path as described in Sect. 4.5.2) in which the NO₂ near-surface concentrations are extended for the six different wavelengths. Generally, the MAX-DOAS horizontal sensitivities are longer for larger wavelengths because of the less pronounced Rayleigh scattering (see also Fig. 6; Ortega et al., 2016; Dimitropoulou et al., 2020). In Fig. 10, the shortest line represents the smallest wavelength's horizontal sensitivity (343 nm), and the longest line the largest wavelength's horizontal sensitivity (530 nm). As can be seen in the sketch, the effective horizontal light path at the six different wavelengths passes through different number of horizontal bins.

The parameterized NO₂ near-surface concentrations at the different wavelengths are the mean concentrations along the horizontal effective light paths (see Section 4.5.2), which are also called differential effective light paths because they are linked to the dSCD_{NO₂}. When having information coming from one wavelength only, it is not possible to know how the NO₂ is distributed along this light path. In the present work, the knowledge of mean NO₂ concentrations at six different wavelengths is used to retrieve a horizontal NO₂ profile, assuming the horizontal box model described in Fig. 10. This new retrieval method is described below.

The measurement vector y consists of the six retrieved surface concentrations (called as \bar{c}_{NO_2} ; see method presented in Sect. 4.5.2) at the six different wavelengths. These near-surface concentrations can be expressed as functions of the different effective light paths (L_{NO_2}) and correspond to the average surface concentrations along those L_{NO_2} :

$$y = \mathbf{F}_{\text{meas}}(c_{\text{NO}_2, \text{true}}) = \bar{c}_{\text{NO}_2} = \frac{\text{dSCD}_{\text{NO}_2}}{L_{\text{NO}_2}} \quad (4.10)$$

$\mathbf{F}_{\text{calcul}}$, which represents the forward model, can be expressed as follows:

500

$$F_{\text{calcul}}(c_{\text{NO}_2, \text{true}}) = \frac{1}{L_{\text{NO}_2}} \int_0^{L_{\text{NO}_2}} c_{\text{NO}_2}(x) dx$$

$$\left(\frac{1}{L_{\text{NO}_2}} \int_0^{L_{\text{NO}_2}} e^{-\frac{x}{L_{\text{NO}_2}}} c_{\text{NO}_2}(x) \frac{dx}{\cos(a)} \right) \quad (11)$$

where x is the horizontal distance, a is the elevation angle of the measurement and c_{NO_2} the NO_2 near-surface concentration as a function of x , the distance from the MAX-DOAS instrument.

505

Our retrieval of the horizontal distribution of c_{NO_2} is based on the inversion theory (Rodgers, 2000), in which a horizontal profile c_{NO_2} (state vector) is retrieved given an a-priori horizontal profile x_a , the measurement vector y , the matrix of the weighting function \mathbf{K} , the uncertainty covariance matrix of the a priori \mathbf{S}_a and the uncertainty covariance matrix of the measurement \mathbf{S}_e :

510

$$c_{\text{NO}_2} = x_a + (\mathbf{K}^T \mathbf{S}_e^{-1} \mathbf{K} + \mathbf{S}_a^{-1})^{-1} \mathbf{K}^T \mathbf{S}_e^{-1} (y - \mathbf{K} x_a) \quad (12)$$

The weighting function indicates the sensitivity of the measurement vector to a change in the horizontal profile. It is given in the present case by the following analytical functions. Following the Beer-Lambert law, the weighting function are following an exponential decrease between the instrument and L_{NO_2} . Additionally, we should consider that the light path through the horizontal boxes is slanted and not horizontal by including the cosine of the elevation angle a (i.e., 2° elevation angle). The weighting functions are given by the following equation:

515

$$K(x, L_{\text{NO}_2}) = \frac{dF_{\text{meas}}}{dc_{\text{NO}_2}} = \begin{cases} \frac{dx}{L_{\text{NO}_2}} & \text{for } 0 < x < L_{\text{NO}_2} \\ \frac{\Lambda dx}{L_{\text{NO}_2}} & \text{for } x(\text{max}) > L_{\text{NO}_2} \\ 0 & \text{for } x > L_{\text{NO}_2} \end{cases} \quad (14)$$

520 where Λ is the coverage percentage of the differential effective light path length at the last horizontal grid $x(\text{max})$.

$$K(\lambda, x) = \frac{1}{L_{\text{NO}_2}} e^{-\frac{x}{L_{\text{NO}_2}}} \frac{\Delta x}{\cos(a)} \quad (13)$$

An example of weighting functions is presented in Fig. 11. As can be seen, the sensitivity decreases exponentially up to a distance corresponding to the differential effective light path length of each measurement. More precisely, each measurement is highly sensitive from the MAX-DOAS instrument location. This sensitivity decreases exponentially as a function of the horizontal distance. Then, it reaches a value equal to $1/e$ to the horizontal distance equal to the differential effective light path length of each measurement. As each last horizontal grid is not fully covered by each measurement, the coverage percentage is considered for these grid cells. It should be noted that since NO_2 is an optically thin absorber, the measurements depend

525

linearly on each horizontal box's concentration. For this reason, OEM for the linear case is considered here, and only one inversion step is needed (see Eq. 4312).

The selected output horizontal grid for the retrieval extends from the MAX-DOAS instrument to the ~~maximum differential effective light path (L_{NO_2} at 530 nm)~~ horizontal distance in which the ~~weighting function of the largest wavelength (i.e., 530 nm) decreases at 10% of its value at the MAX-DOAS instrument's location~~ per azimuthal direction and consists of successive boxes of 0.5 km thickness on the horizontal axis.

Since this inversion problem is ill-conditioned, more than one horizontal NO_2 profile can be consistent with the measurement vector. To reject unrealistic solutions, the a priori profile \mathbf{x}_a and its uncertainty covariance matrix must be included in the retrieval. In the OEM, the a priori information usually comes from an independent source, like a model or other correlative measurements. In the present study, RIO model data were chosen as a priori. ~~RIO is a land-use regression model based on the interpolation of the hourly NO_2 near-surface concentrations measured by the in-situ telemetric air quality network in Belgium (Hooyberghs et al., 2006; Janssen et al., 2008). RIO provides hourly NO_2 concentration maps on a 4×4 km² spatial resolution.~~

Seasonal average maps of RIO NO_2 near-surface concentration are constructed (see Fig. S3) and after, seasonal averages of RIO NO_2 near-surface concentration horizontal profiles were calculated in each azimuthal direction and interpolated on the retrieval's horizontal grid by regridding the initial 4×4 km² spatial resolution to a finer one (see Fig. 12). The shape of the RIO a priori NO_2 profiles per azimuthal direction stays the same during different seasons of the year, indicating that the wind effect on NO_2 transportation disappears by the seasonal averaging and that the same sources contribute to the NO_2 horizontal field.

A mean scaling factor equal to the mean ratio between the measured and RIO NO_2 near-surface concentrations is applied because of the systematic underestimation of NO_2 near-surface concentrations by MAX-DOAS when compared to in-situ measurements (see Dimitropoulou et al., 2020 and Section S1).

For the aerosols horizontal distribution retrieval, there are not sufficient independent measurements that provide information about the horizontal distribution of AOD and can serve as an a priori AOD profile. Therefore, a ~~linearly decreasing constant~~ a priori AOD profile is used in the AOD retrieval based on CIMEL observations. An AOD equal to 0.18, which is the yearly-averaged AOD value from CIMEL at 477 nm, is used ~~close to the MAX-DOAS instrument with a linear decrease as we move away from the instrument.~~ To construct the near-surface aerosol extinction a priori profiles, it is considered that 30% of the total amount of AOD is located inside the MLH (i.e., known for each MAX-DOAS vertical scan from the MMF inversion algorithm; see Section 45.1).

The diagonal elements of the \mathbf{S}_a matrix are set equal to the square of a scaling factor times the NO_2 concentration a priori profile. The non-diagonal elements, which account for correlation between the different horizontal grid cells, are set as follows (Barret et al., 2002):

$$\mathbf{S}_{a_{ij}} = \sqrt{\mathbf{S}_{a_{ii}} \mathbf{S}_{a_{jj}}} \exp\left(-\ln(2) \left(\frac{x_i - x_j}{Y}\right)^2\right) \quad (4514)$$

560

where x_i and x_j are the horizontal distances at the i^{th} , and j^{th} horizontal boxes and γ is half of the correlation length. For NO_2 , γ is set equal to 3.5 km and for aerosols, γ is set equal to 2 km. To eliminate inversion instabilities, S_a elements which are smaller than 0.1% of the maximum S_a element are set equal to zero.

To estimate the correlation length, a covariance matrix was constructed by exploiting the airborne observations above Brussels (28 June 2019). The airborne observations have a spatial resolution of approximately $100 \times 100 \text{ m}^2$. NO_2 horizontal profiles were constructed in different azimuthal directions in a spatial resolution of $500 \times 500 \text{ m}^2$, expanding from the MAX-DOAS's position to a maximum distance of 20 km, and were used to calculate a covariance matrix. A correlation length equal to 7 km, and consequently, a gamma value equal to 3.5 km, is found to be representative for the NO_2 horizontal profiles in Brussels.

Using this correlation length, a variance of 45% is used. This choice was conducted based on the seasonal variance of the RIO a priori profiles compared to their seasonal mean value. It is found that the seasonal variance of RIO observations has a mean value of 45%. Additionally, it is found to be a good compromise for obtaining reasonable retrieval results e.g. in terms of information content, and while avoiding unrealistic oscillations in the retrieved aerosol and NO_2 profiles. It should be noted that for aerosols, a variance of 65% is used.

The measurement covariance matrix S_e is chosen to be diagonal, with elements corresponding to the uncertainties of the dual-scan parameterized NO_2 near-surface concentration (see Section 4.2.2).

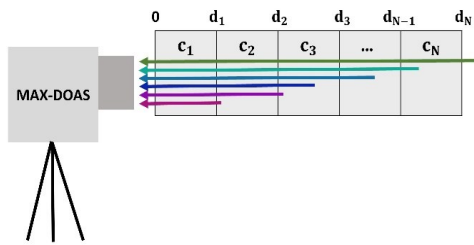
Three examples of the retrieved NO_2 horizontal profile are presented in Fig. 13, together with corresponding measured and simulated \bar{c}_{NO_2} at the six different wavelengths for July 2, 2018 (Fig. 13a; low NO_2 abundance condition), September 11, 2018 (Fig. 13b; medium NO_2 abundance condition), and September 30-2018, 2018 (Fig. 13c; medium NO_2 abundance condition).

RMS is calculated between measured and simulated NO_2 near-surface concentrations of the horizontal retrieval normalized by the mean of the measured NO_2 near-surface concentrations (upper panels in Fig. 13). For distances smaller than the minimum L_{NO_2} (around 8 km), the measurements do not give information about the horizontal distribution of NO_2 . Consequently, the retrieved NO_2 horizontal profile at these ranges is coming from the a priori profile. Similarly, the measured and retrieved near-surface aerosol extinction coefficient and the retrieved aerosol horizontal profile are shown in Fig. 14, for three sample cases. As the NO_2 values become larger, the agreement between measured and simulated \bar{c}_{NO_2} , expressed via the RMS value, is improved.

Similarly, examples of measured and retrieved near-surface aerosol extinction coefficient and retrieved aerosol horizontal profile are shown in Fig. 14, for different aerosol load conditions (low (Fig. 14a), medium (Fig. 14b) and high (Fig. 14c)) over the Brussels-Capital Region. We observe that the agreement between simulated and measured near-surface aerosol extinction coefficient at the six different wavelength tends to be worse than for NO_2 . This could be due to the use of a constructed (constant) a priori aerosol horizontal profile due to the lack of information on the aerosol extinction horizontal distribution in the Brussels-Capital region.

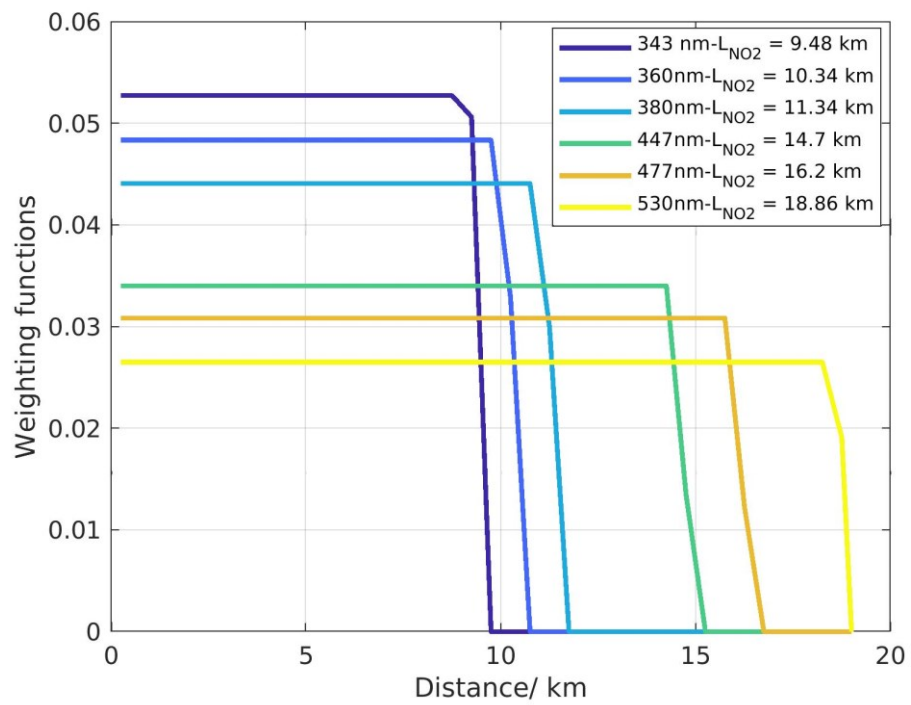
An essential condition of the dual-scan MAX-DOAS retrieval and the new horizontal inversion approach at six different wavelengths is the increasing trend of the horizontal sensitivity as a function of wavelength. Consequently, every wavelength is sensitive to a different horizontal region and the six different wavelengths can be used to retrieve the horizontal distribution

595 of aerosols and trace gases. Sensitivity tests were conducted in which simulated L_{O_4} are expressed as a function of the six
different wavelengths for different aerosol conditions. As can be seen in Fig. S4, the linear relationship between L_{O_4} (and L_{NO_2})
and wavelength exists for AOD values ranging from 0 to 1. An AOD equal to unity is chosen as the maximum AOD of the
simulations because in Uccle, AOD values rarely exceed one (see in <https://aeronet.gsfc.nasa.gov/> for the Brussels
measurement site). Therefore, the relation stays linear as the aerosol load changes for the conditions observed in Uccle. The
600 only condition leading to non-linearity is when clouds are present. However, as explained in Sect. 4.5.1, a cloud filtering
approach is applied, rejecting the broken cloud scenes, which are the more problematic ones.



605 **Figure 10. Schematic representation of the six different L_{NO_2} (i.e., one horizontal line for each wavelength) used in the
new horizontal distribution inversion approach. The length of each line shows the sensitivity of each wavelength as a
function of the horizontal distance. The shortest line represents the smallest wavelength.**

610



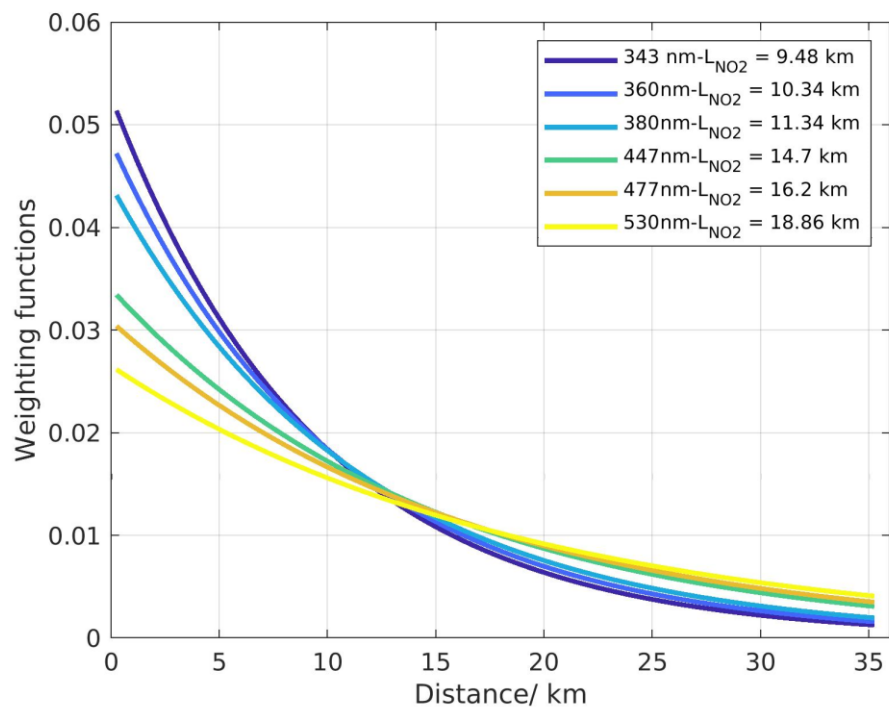
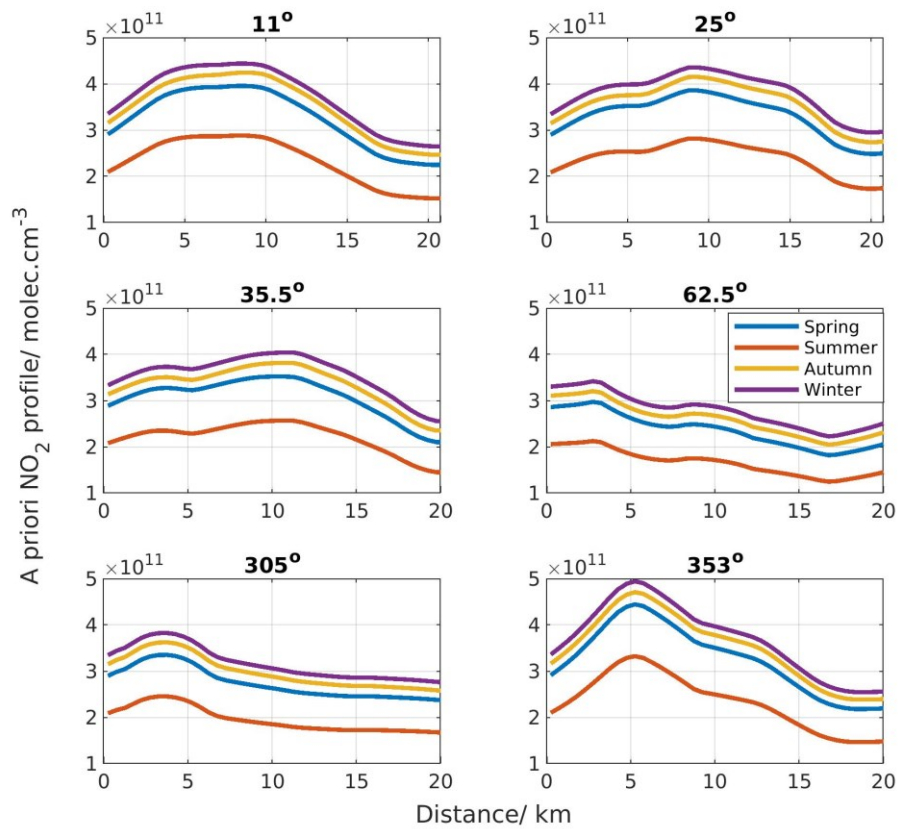


Figure 11. Examples of weighting functions used in the new horizontal distribution inversion approach (11 September

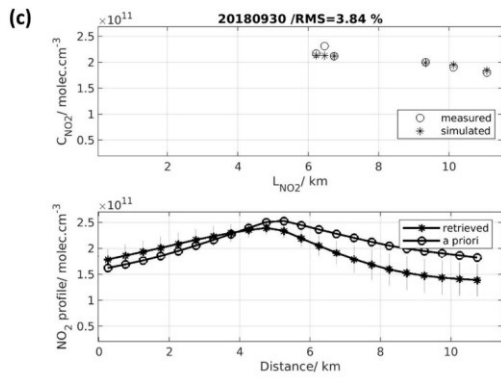
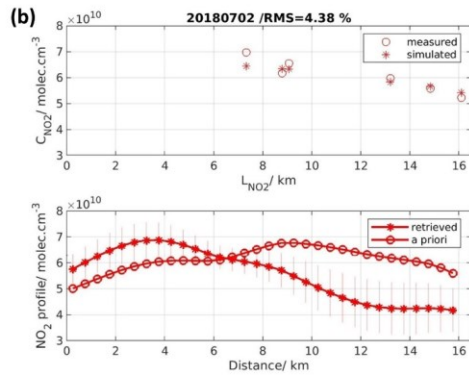
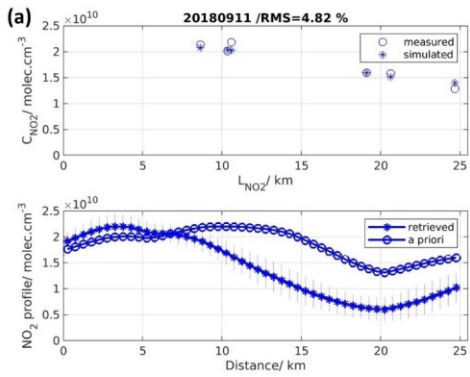
615 2018, 11:26 UTC).

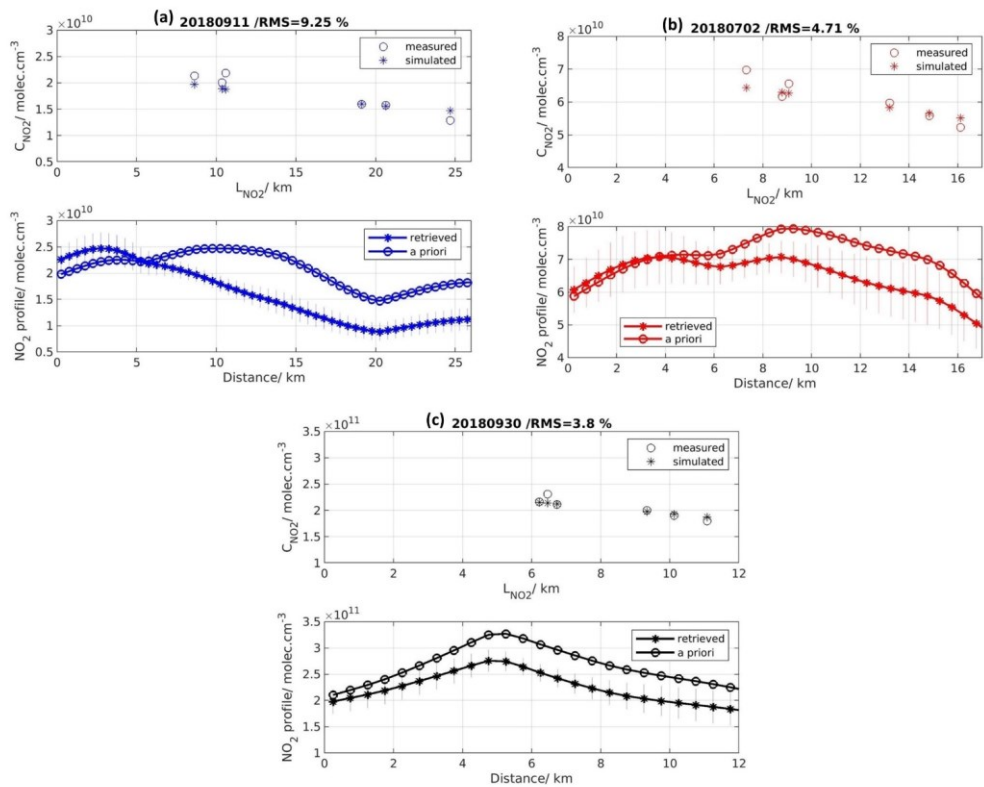
620



625 **Figure 12. Example of seasonal RIO *a priori* NO₂ horizontal profiles for the new horizontal distribution inversion approach as a function of the horizontal distance from the MAX-DOAS instrument in six different azimuthal viewing directions, before the application of the scaling factor.**

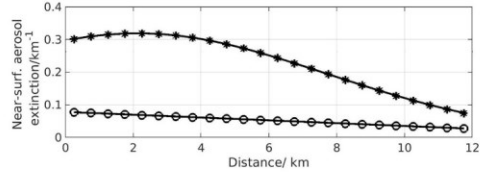
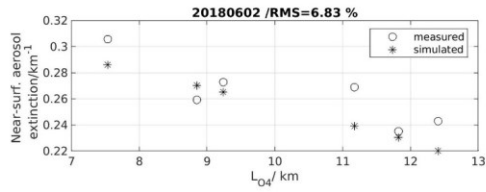
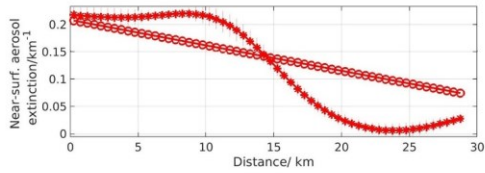
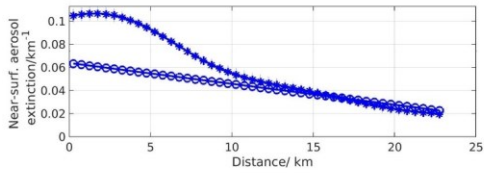
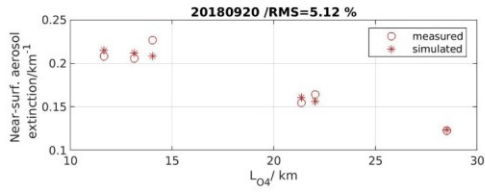
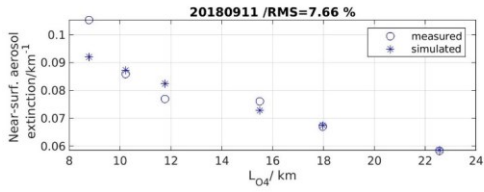
630





635 **Figure 13.** (Upper panels in a, b, and c) Measured and retrieved NO₂ near-surface concentrations at the six different wavelengths (i.e., horizontal distances) as a function of the estimated horizontal distances and (lower panels in a, b, and c) the retrieved NO₂ near-surface horizontal profile and a priori profile. The two panels correspond to the (a) 11 September 2018, 12.91 UTC, 265° azimuthal direction, (b) 02 July 2018, 10.42 UTC, 25° azimuthal direction, and (c) 30 September 2018, 07.96 UTC, 167.5° azimuthal direction.

640



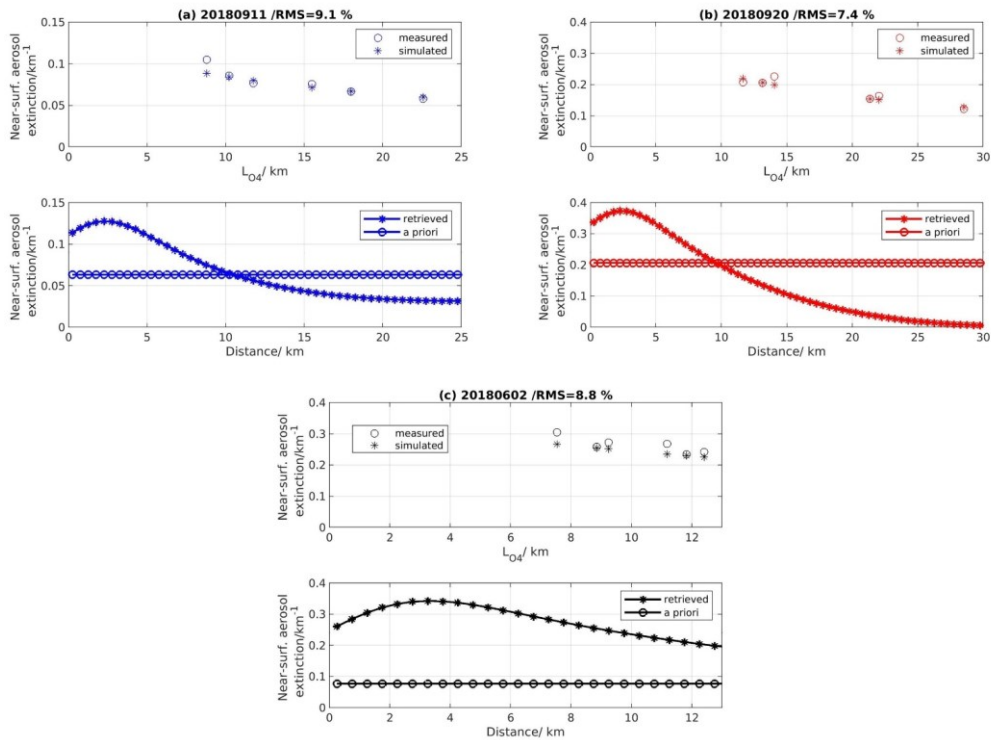


Figure 14. (Upper panels in a, b, and c) Measured and retrieved near-surface aerosol extinction at the six different wavelengths (i.e., horizontal distances) as a function of the estimated horizontal distances and (lower panels in a, b, and c) the retrieved near-surface aerosol extinction horizontal profile. The two panels correspond to the (a) 11 September 2018, 11.48 UTC, 167.5° azimuthal direction, (b) 20 September 2018, 07.08 UTC, 25° azimuthal direction, and (c) 02 June 2018, 18.16 UTC, 35.5° azimuthal direction.

655 4.4 Characterization of the retrieval

To characterize the retrieval, the averaging kernels, **AK**, play a crucial role. The **AK** matrix is calculated as follows (Rodgers, 2000):

$$AK = \frac{dc_{NO_2}}{dc_{NO_2, true}} = (K^T S_e^{-1} K + S_a^{-1})^{-1} K^T S_e^{-1} K \quad (1615)$$

660

The **AKs** are the rows of the **AK** matrix. They present the sensitivity of the retrieved (c_{NO_2}) on the true ($c_{NO_2, true}$) atmospheric profile. Ideally, the **AK** matrix should be an identity matrix. In Fig. 15, an example of selected **AKs** is shown. As can be seen, for distances smaller than the first measurement (e.g., near-surface NO_2 concentration retrieved at 343 nm), the **AKs** are constantly zero (or have small maximum values) and decrease exponentially as a function of the horizontal distance from the MAX-DOAS instrument until these distances. This indicates a low sensitivity on these short distances, and therefore information about the horizontal distribution of NO_2 is coming essentially from the a priori profile. The **AKs** create a maximum flat plateau close to their nominal horizontal distance for larger distances ($d=8.75$ km, $d=10.25$ km, and $d=24.75$ km). For this particular example, the **AKs** do not exceed the values of 0.0612.

665

670

Another important information about the retrieval is the trace of the **AK** matrix, which refers to the number of degrees of freedom for signal (DOFS). The DOFS are an indication of the number of independent pieces of information that one can retrieve from the measurements. Ideally, the DOFS would be equal to the number of horizontal boxes for the horizontal distribution. In reality, the DOFS are lower, because of the limited horizontal resolution of the measurements. In Fig. 15, the DOFS are close to two, which means that two independent pieces of information are contained in the measurements for this particular example.

675

In the present work, the total retrieval error is equal to the error related to the measurement noise and the smoothing of the true atmospheric profile. According to Rodgers (2000), the retrieval noise error covariance matrix is estimated as:

$$S_{meas} = G S_e G^T \quad (1716)$$

680

with, G being the gain matrix:

$$G = (K^T S_e^{-1} K + S_a^{-1})^{-1} K^T S_e^{-1} \quad (1817)$$

Then, the retrieval noise error is given as the square root of the diagonal elements of the noise covariance matrix.

The smoothing error is calculated as follows:

$$S_{smooth} = (AK - I) S_x (AK - I)^T \quad (1918)$$

685

with S_x being a realistic covariance metric of the true NO_2 horizontal profile.

The horizontal profiles of the measurement and smoothing error in percentage are shown in Fig. 16. As can be seen, the measurement error becomes maximum for the longest distance. As can be seen, the smoothing error is significantly larger than the measurement error (range of 3%-10% and 14%-40%, respectively). The smoothing error becomes also larger as the horizontal distances from the instrument become larger. This is mainly because of the exponential decrease of the sensitivity

Formatted: English (United Kingdom)

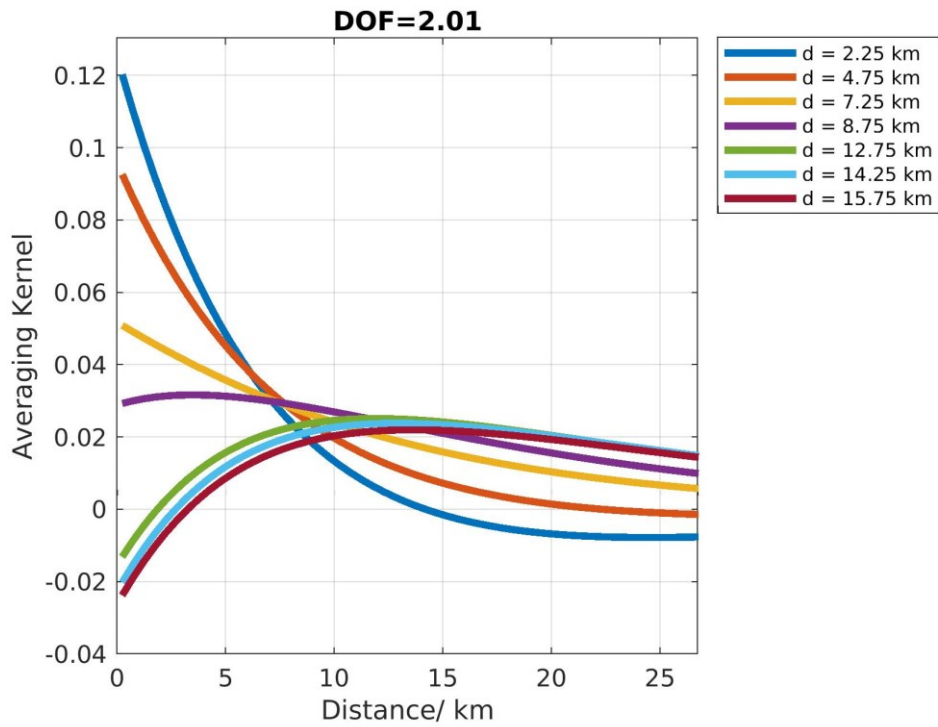
as a function of the horizontal distance (see weighting functions in Fig. 11), and consequently, the larger impact of the difference between the a priori profile and the true state of the atmosphere.

To eliminate the unsuccessful retrievals, the percentage of accepted retrievals with respect to the total number of retrievals during the four seasons is investigated when a specific filtering on RMS and DOFS is applied (see Table 3 and Figures S7 and S8). As we can see in Fig. S8, DOFS are in the range of 1.2-2.50-1.6. From these tests, it is found that most of the retrievals have DOFS larger than 1.52 (see Fig. S8). RMS is defined as the root-mean-square deviation between measured and simulated c_{NO_2} normalized by the mean of the measured c_{NO_2} (e.g., same RMS as in Fig. 13). Table 3 and Fig. S7 indicate that RMS values are in the range of 0-30% and most of the retrievals have an RMS smaller than 69% with a median RMS value of around 4.5,6% during all seasons. Based on these investigations, $DOFS > 1.52$ and $RMS < 69\%$ are used as retrieval quality control criteria.

Formatted: Font color: Red, English (United Kingdom)

Table 3. Seasonally averaged root-mean-square (RMS) and DOFS values. RMS is calculated between measured and retrieved NO₂ near-surface concentrations of the horizontal retrieval (Fig. 13). DOFS represent the degrees of freedom of the horizontal retrieval (Fig. 15). The percentage of the accepted retrievals is presented for the different selection criteria.

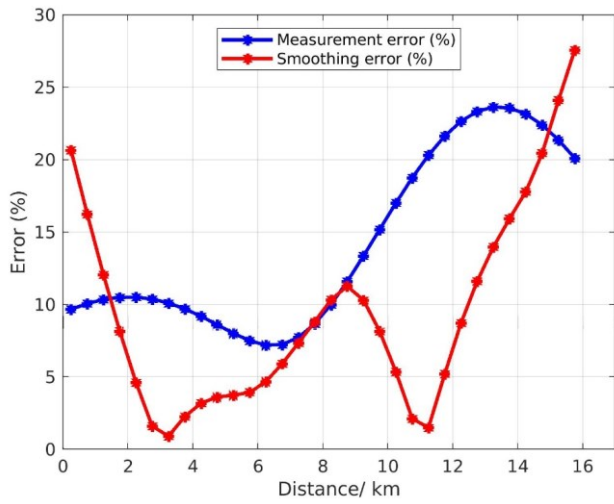
Season	Spring	Summer	Autumn	Winter
Median RMS (%)	34.8	4.7 7.2	4.75,1	5.4,8
Median DOFS	1.73	1.73	1.63	1.63
Accepted retrievals (%) (DOFS > 1.52)	90 87	91 72	81 70	78 73
Accepted retrievals (%) (RMS < 9%)	75	80	94	55
Accepted retrievals (%) (RMS < 8%)	56	71	68	32
Accepted retrievals (%) (RMS < 7%)	27	68	57	11
Accepted retrievals (%) (RMS < 6%)	80,89	55		57
Accepted retrievals (%) (RMS < 5%)	83	33,59	49	83
Accepted retrievals (%) (RMS < 4%)	75	47	36	85
Accepted retrievals (%) (RMS < 3%)	66	11	15	74
	65	67	57	65

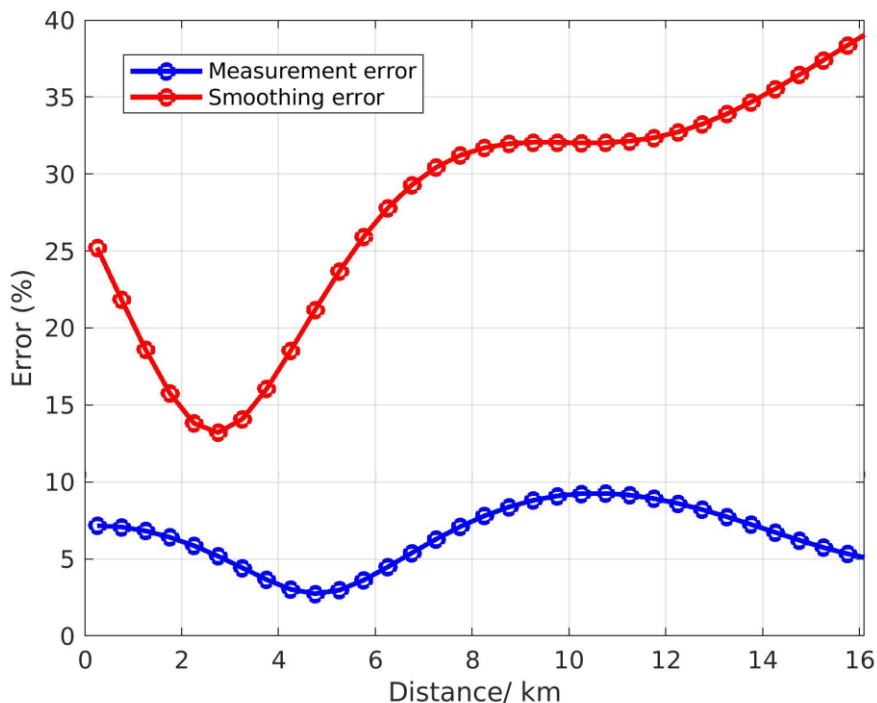


715

Figure 15. Example of NO₂ averaging kernels. They are calculated for observations on 11 September 2018 at 11:51 UTC and 300° azimuthal direction.

720





725 **Figure 16.** Example of the NO₂ measurement and smoothing error in percentage for the 02 July 2018 at 10.42 UTC and 25° azimuthal direction.

5.6 Retrieval results and discussion

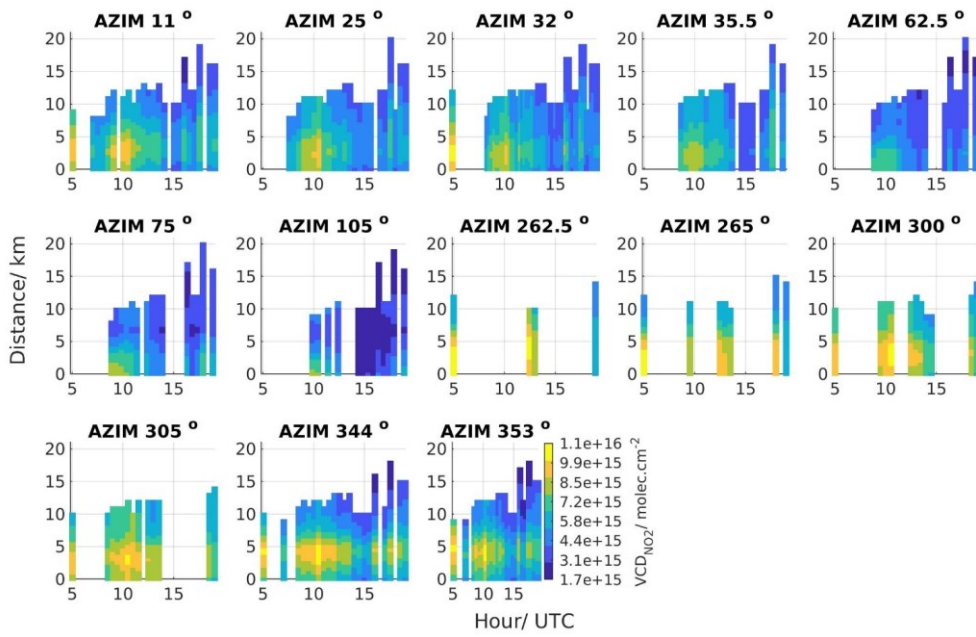
5.6.1 Example of daily horizontal NO₂ distribution

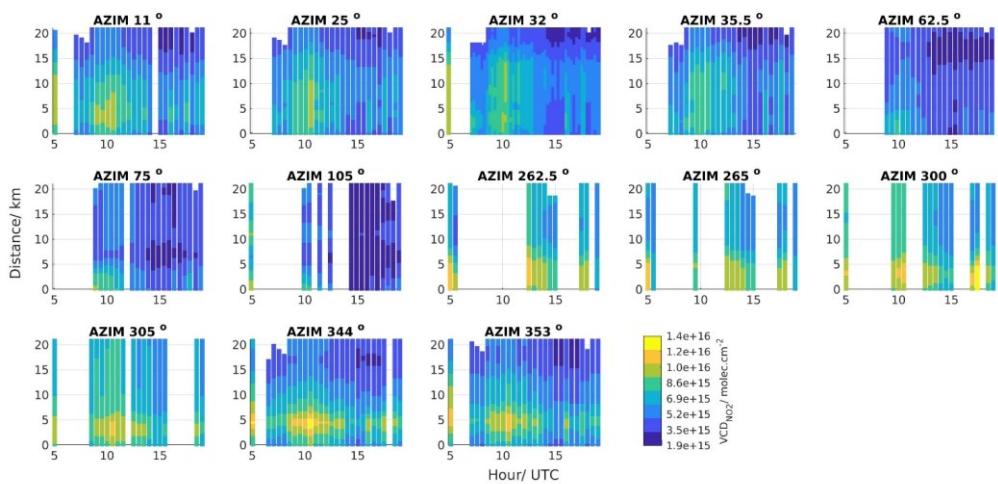
730 The variation of the MAX-DOAS horizontal distribution of tropospheric NO₂ VCDs as a function of time over the course of June 28 2019, is presented in Fig. 17. This particular day is chosen because airborne measurements took place above the Brussels region (see Sect. 5.6.2). The horizontal NO₂ profiles are plotted per azimuthal direction with the horizontal axis showing the time in UTC and the vertical axis the horizontal distance in km. Because of the quality check on the retrieved NO₂ horizontal profiles (see Sect. 4.5.3), some profiles were rejected (e.g. azimuthal direction equal to 262.5° and 265°).

735 During this day, maximum NO₂ columns are mainly observed around 05:00 UTC and 10:00 UTC, which correspond to 7am
and noon local time. Early in the morning (05:00 UTC), high NO₂ columns are expected to be observed because of the low
MLH (MLH_{NO₂} in the range of 300 – 600 m height) in combination with the morning rush hour NO₂ emissions. Around 10:00
UTC, the maximum NO₂ columns are detected in the north (N), northeast (NE), and northwest (NW) direction (see Fig. 18).
Same NO₂ horizontal distribution is found when investigating the NO₂ near-surface concentrations for this day (see Fig. S5).
740 In the Brussels region, the main emission sources are located in the N and west (W) parts of the city and are linked to the
motorway around Brussels (the so-called Ring), the Brussels city center, and the Drogenbos power plant (NW direction).
Concerning the NO₂ peaks, they are located at a distance around 0 to 8 km from the measurement site. It can be seen from Fig.
18 that the Ring, the Brussels city center, and the Drogenbos power plant are located within these distances. As measured by
the meteorological station on the BIRA-IASB rooftop, the wind was coming from the E direction during that day, resulting in
745 the progressive displacement of the NO₂ peak from the NNE to the W direction. On the contrary, the azimuthal directions
pointing towards a large forested area (i.e., 62.5°, 75°, and 105°), the Bois de la Cambre, detect considerably lower NO₂
columns than the other directions.

Maximum near-surface aerosol extinction coefficient values are observed during all day long and detected in the N, NW and
NE direction (see Fig. S6). NO₂ and aerosol peaks are co-located towards the N and NW direction.

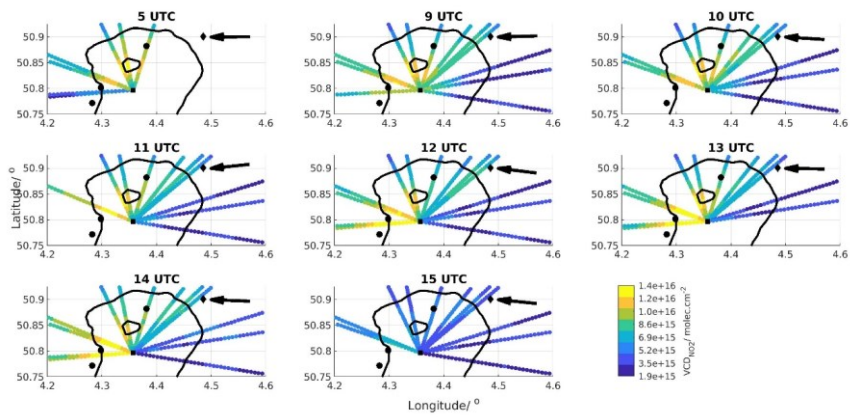
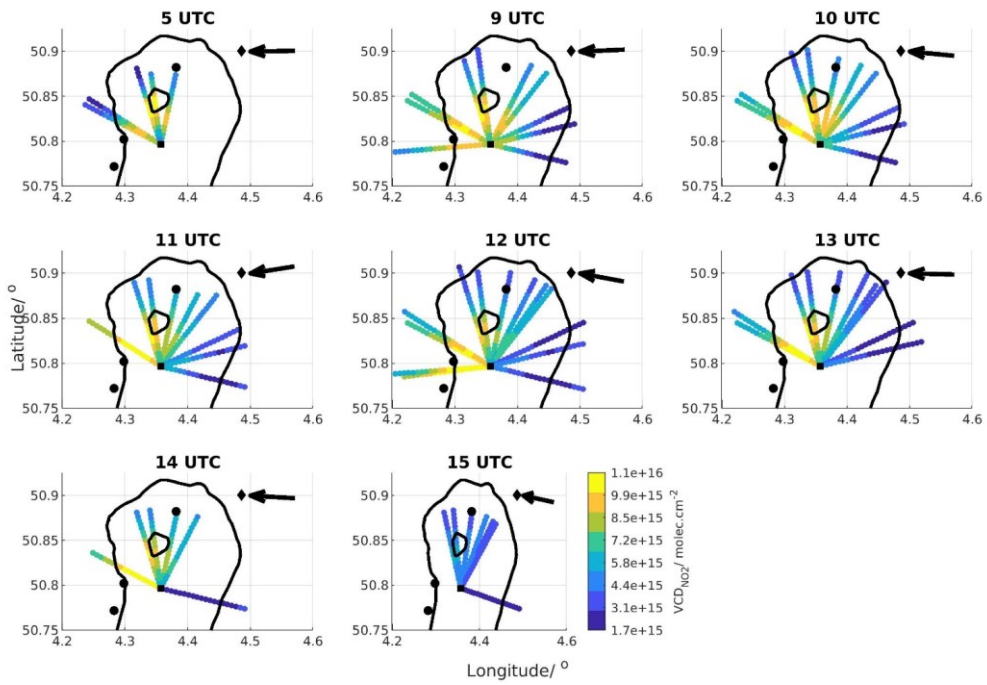
750





755 **Figure 17. Diurnal variation of the retrieved NO₂ horizontal profiles per azimuthal direction as a function of time (UTC) for June 28, 2019.**

760



765 **Figure 18. Maps of hourly averaged NO₂ horizontal profiles per azimuthal direction for June 28, 2019 corresponding to Fig. 17. The wind direction is shown with the black arrow. The black square shows the MAX-DOAS instrument location, the black polygon the National Airport, the black dots the NO₂ hotspots emitting more than 10 kg of NO_x per hour (Emission Inventory of the Belgian Interregional Environment Agency, 2017) , and the black line represents the Brussels Ring road.**

770 **5.6.2 MAX-DOAS horizontal NO₂ distribution versus airborne, car mobile-DOAS, and TROPOMI: 28 June 2019 case study**

775 ~~For the SSP validation campaign over Belgium (SSPVAL-BE, <https://ssp.campaigns.aeronomie.be/>), airborne measurements of the two largest urban regions over Belgium, i.e., Antwerp and Brussels, took place from 26 to 29 June 2019 (Tack et al., 2021). The Airborne Prism EXperiment (APEX) imaging spectrometer was used to measure the horizontal distribution of tropospheric NO₂ columns with a spatial resolution of approximately 75 m x 120 m (Tack et al., 2017; Tack et al., 2019).~~

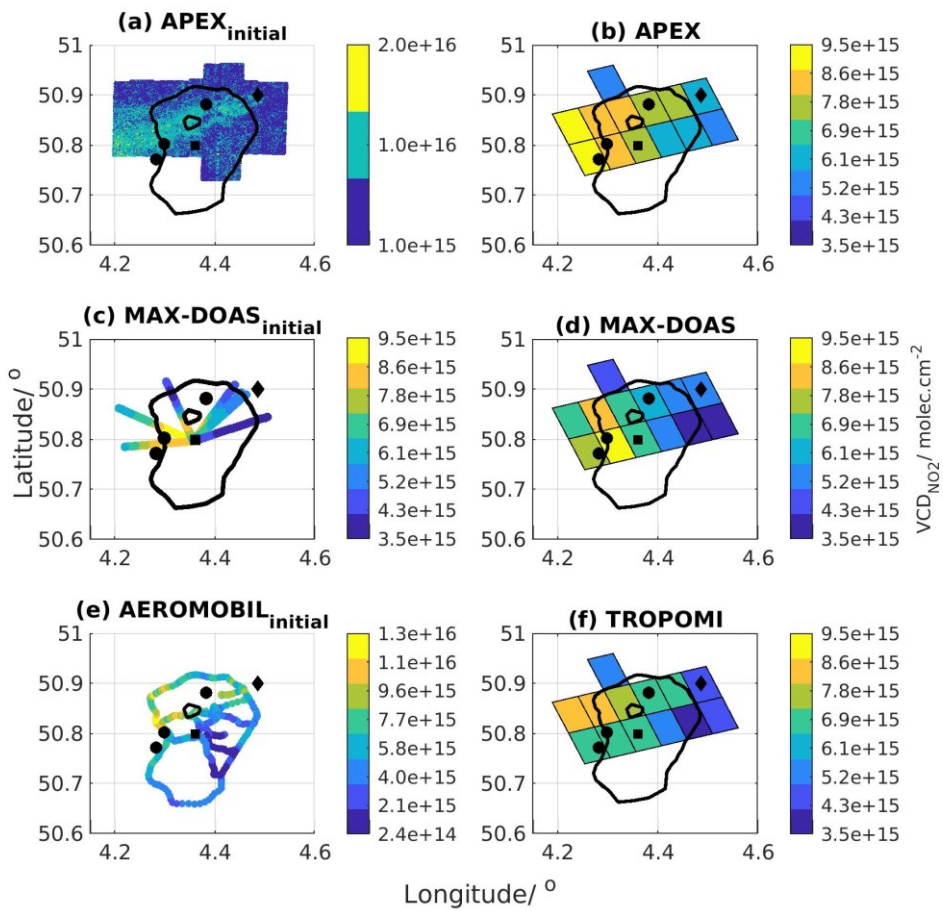
780 The APEX tropospheric NO₂ columns are compared to the tropospheric NO₂ horizontal distribution as retrieved by applying our new mapping MAX-DOAS technique to the 28 June 2019 measurements. During the same day, TROPOMI pixels (OFFL 010302 product; see Table 1) selected over the Brussels region are compared to MAX-DOAS observations. During this day, the TROPOMI overpass time was at 12:19 UTC. MAX-DOAS horizontal profiles of tropospheric NO₂ VCDs are selected around TROPOMI overpass time (± 1 hour). The horizontal profile of MAX-DOAS NO₂ VCDs on each horizontal line-of-sight has a horizontal sampling of 0.5 km (see Fig. 13). The MAX-DOAS NO₂ VCDs on the horizontal segment crossing a TROPOMI pixel and located inside the pixel are averaged and compared to the corresponding TROPOMI NO₂ VCD. It should be noted that the MAX-DOAS segments are weighted by their relative length inside each pixel. APEX observations located inside each TROPOMI pixel were used to assign one APEX NO₂ VCD value per pixel. Maps of co-located TROPOMI, AEROMOBIL, averaged MAX-DOAS, and averaged APEX NO₂ VCDs for the 28 June 2019 are shown in Fig. 19. Two maps of APEX and MAX-DOAS observations are presented: one with APEX and MAX-DOAS in their initial resolution and one with spatially averaged APEX and MAX-DOAS observations in the area covered by a TROPOMI pixel. The NO₂ plume as detected by APEX is covering the NW, N, and NE parts of the Brussels region. MAX-DOAS successfully detected the same NO₂ plume in the NW and N but not in the NE direction. The correlation and agreement between APEX and MAX-DOAS observations is very good ($R=0.84$ and $s=1.15$). As we can observe in Fig. 20, the APEX tropospheric NO₂ VCDs tend to be larger than the MAX-DOAS ones, with an intercept equal to -2.36×10^{15} molec.cm⁻².89 and $s=1.22$).

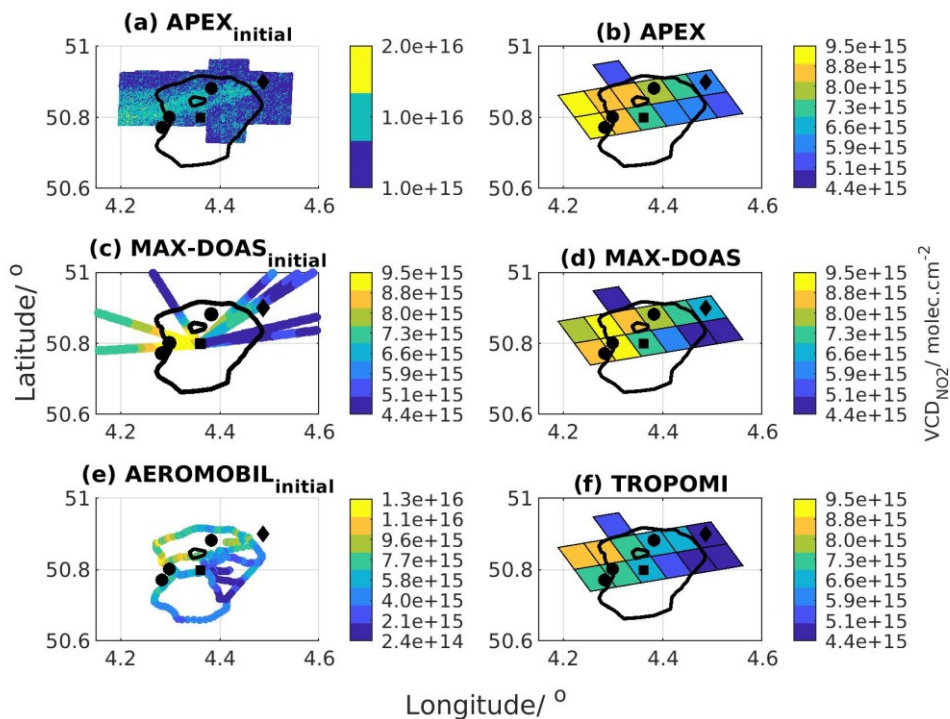
795 ~~During the SSPVAL-BE flight over Brussels, the AEROMOBIL was used to measure the spatial distribution of tropospheric NO₂ columns mainly over the Ring road of Brussels. During the SSPVAL-BE flight over Brussels, car mobile-DOAS observations were performed by the BIRA-IASB mobile-DOAS, the so-called AEROMOBIL (Merlaud, 2013). The AEROMOBIL consists of a compact double Avantes spectrometer recording simultaneously scattered light in two elevation~~

Formatted: Font color: Auto

angles (i.e., one at 30° elevation angle and one at zenith). The AEROMOBIL was used to measure the spatial distribution of tropospheric NO₂ columns mainly over the Ring road of Brussels with start measurement time at 8:30 UTC and end time at 15:42 UTC. The AEROMOBIL NO₂ VCDs, which are located closest both in time and space to each MAX-DOAS horizontal grid are compared to the corresponding MAX-DOAS VCDs (see Fig. 19c and 19e). AEROMOBIL and MAX-DOAS agree perfectly on the location of maximum (i.e. NW direction) and minimum (i.e. SE direction) NO₂ tropospheric VCDs (Fig. 19c and 19e). We can observe in Fig. 20b, that the correlation coefficient is moderate (R equal to 0.7479) and the slope value is equal to 0.5559. The correlation plot between both datasets reveals that AEROMOBIL gives higher NO₂ tropospheric VCDs compared to MAX-DOAS ones. This finding could be partly explained by the fact that AEROMOBIL follows busy routes, where the NO₂ tropospheric VCDs reach maximum values because of the contribution of NO₂ production resulted by vehicles' engines via fossil fuel combustion.

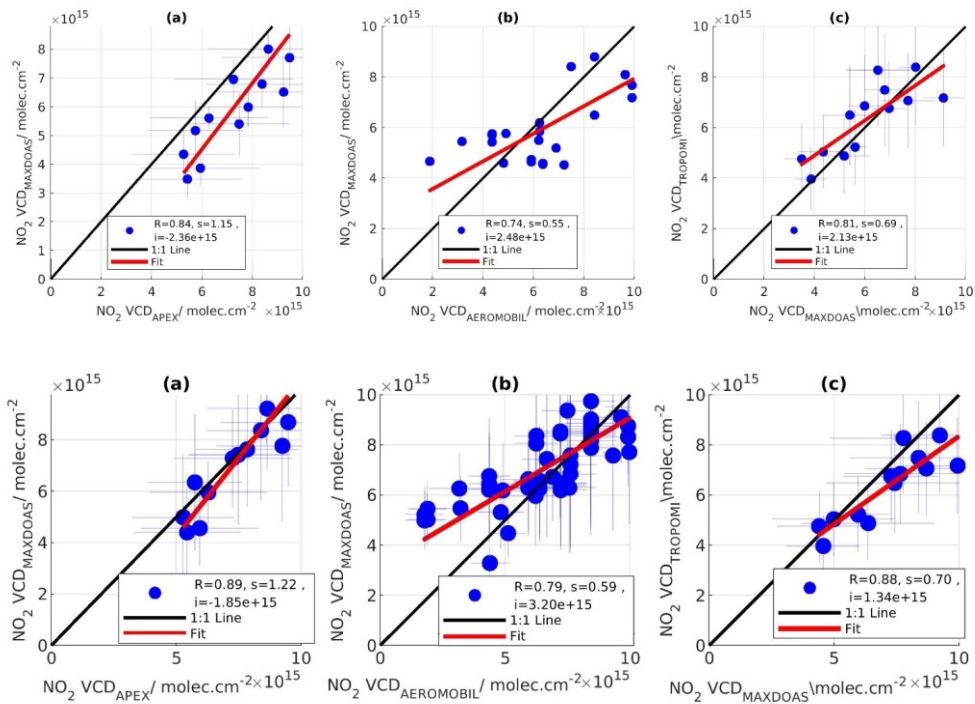
During the TROPOMI overpass (i.e., 12:19 UTC) above the Brussels-Capital Region, dual-scan MAX-DOAS tropospheric NO₂ columns are retrieved, as it can be seen in Fig. 18. The correlation between TROPOMI and MAX-DOAS tropospheric NO₂ columns during the day of the airborne measurements above Brussels is presented in Fig. 20c. Excellent agreement is obtained, with a correlation coefficient value equal to 0.8188. The slope value is equal to 0.6970. During that day, MAX-DOAS and TROPOMI are in good agreement but TROPOMI tends to underestimate the tropospheric NO₂ columns. It should be noted that during that day, the range of observed NO₂ VCDs is from 34.4×10^{15} to 8.0×10^{15} to 9.5×10^{15} molec.cm⁻², as retrieved by the MAX-DOAS observations.





825 Figure 19. (a) Tropospheric NO₂ VCD as detected by the APEX instrument in its initial spatial resolution. Tropospheric
 NO₂ VCD maps (TROPOMI pixels) as retrieved over Brussels on 28th of June 2019 by the (b) APEX, (d) MAX-DOAS
 and (f) TROPOMI (overpass time at 12:19 UTC) instruments. Tropospheric NO₂ VCD as retrieved by the (c) MAX-
 DOAS and (e) AEROMOBIL (between 8:30 UTC and 15:42 UTC) in its initial spatial resolution. The black square
 shows the MAX-DOAS instrument location, the black polygon the National Airport, the black dots the NO₂ hotspots
 830 emitting more than 10 kg of NO_x per hour (Emission Inventory of the Belgian Interregional Environment Agency,
 2017), and the black line represents the Brussels Ring road.

835



840 Figure 20. Scatter plot between (a) the tropospheric NO_2 columns derived by airborne measurements (APEX) and the MAX-DOAS observations, (b) the tropospheric NO_2 columns derived by car mobile-DOAS measurements (AEROMOBIL), and the MAX-DOAS observations and (c) the tropospheric NO_2 columns derived by MAX-DOAS observations and the TROPOMI tropospheric NO_2 columns over Brussels on 28th of June 2019.

845

6.3 ~~5.3~~ Comparison of ~~between~~ MAX-DOAS horizontal NO₂ distribution ~~versus~~ and TROPOMI observations

850 To compare the TROPOMI and MAX-DOAS tropospheric NO₂ columns, the ~~following 5 steps~~ similar approach is used, similarly as in Section ~~5.6.2~~:

1. ~~Only MAX-DOAS horizontal profiles of tropospheric NO₂ VCDs retrieved around (±1 hour). Additionally, TROPOMI overpass time are selected.~~
2. ~~The time coincident MAX-DOAS tropospheric NO₂ VCD horizontal grids from all the azimuthal directions are spatially averaged (i.e. one MAX-DOAS mean NO₂ VCD value per pixel) within the overlapping TROPOMI pixels.~~
3. ~~The MAX-DOAS segments are weighted by their relative length inside each TROPOMI pixel.~~
4. ~~The horizontal profiles of MAX-DOAS NO₂ columns have a horizontal sampling of 0.5 km in every azimuthal direction. The coverage percentage is estimated as the ratio of the area covered by MAX-DOAS (i.e., number of coincident MAX-DOAS NO₂ VCDs considering that every MAX-DOAS horizontal grid has a spatial resolution of 0.5 x 0.5 km²) inside each TROPOMI pixel to the total number of MAX-DOAS NO₂ VCDs that could fill in the TROPOMI pixel.~~
5. ~~TROPOMI and MAX-DOAS tropospheric NO₂ columns are compared in a seasonal basis, and the seasonally-averaged maps of those VCDs on the area covered by the TROPOMI pixels are created. To generate these maps, the ensemble of TROPOMI pixels recorded on 28 June 2019 is chosen as reference and TROPOMI pixels that coincide with this reference grid are averaged. The daily horizontal profiles of MAX-DOAS NO₂ columns are averaged on the daily TROPOMI grids and then, the reference grid is used to create the seasonally-averaged MAX-DOAS maps.~~

The seasonally and annually-averaged maps of TROPOMI and MAX-DOAS NO₂ VCDs are presented in Fig. 21 and Fig. 22. Only pixels including at least 20 comparison days are taken into account in the analysis. It is found that the locations of the NO₂ peaks and dips show a reasonably high degree of similarity between TROPOMI and MAX-DOAS during all seasons, except summer. The NO₂ peaks appear mainly above Brussels city center, the Drogenbos power plant (W direction) and the NW part of the Ring road, which are the main known emission sources, as mentioned earlier. These maps also indicate that the tropospheric NO₂ column over the Brussels area has a clear seasonal cycle, with a maximum during winter. Figure 22c shows the annual relative biases (e.g., 100 x (TROPOMI – MAX-DOAS)/MAX-DOAS) per pixel. It is found that ~~positivencgative~~ biases (i.e. ~~TROPOMI, MAX-DOAS~~ larger than ~~MAX-DOAS~~) are observed mainly in the pixels located away ~~TROPOMI~~, ranging from the measurement site during all seasons, while negative biases ~~-3% to -38%~~, are found close to the measurement site and in the Brussels city center ~~for all the pixels~~.

The seasonal correlation plots for April 2018-February 2020 are displayed in Fig. 23. ~~When all pixels are included, without any TROPOMI pixels coverage percentage filtering on MAX-DOAS data, the~~ The highest correlation is found during spring

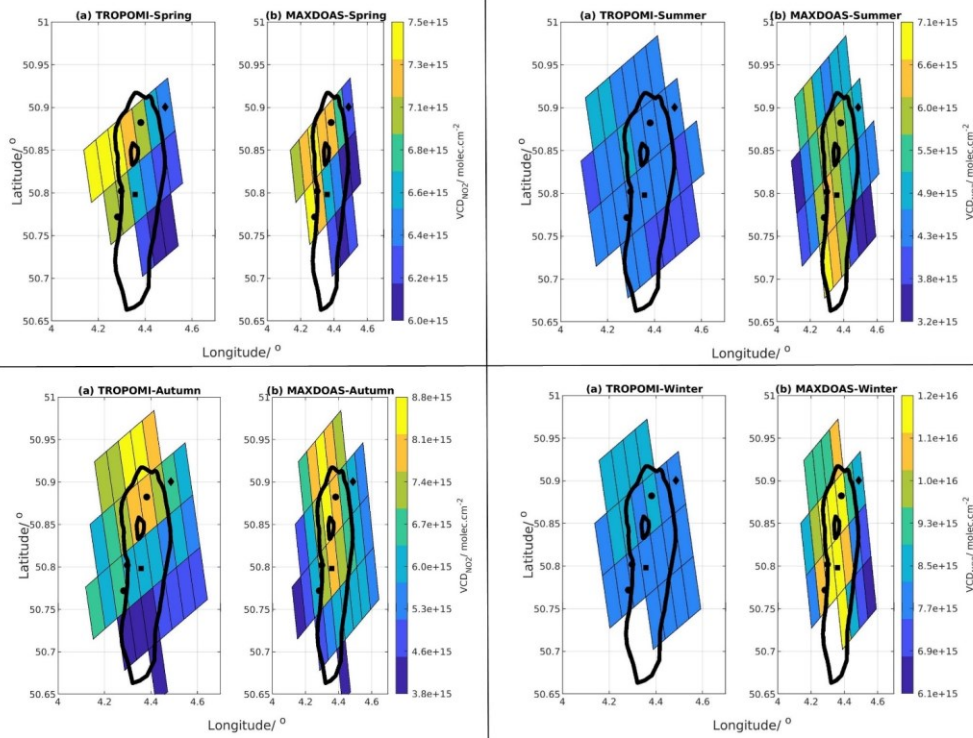
Formatted: Outline numbered + Level: 2 + Numbering Style: 1, 2, 3, ... + Start at: 3 + Alignment: Left + Aligned at: 0 + Indent at: 0,63 cm

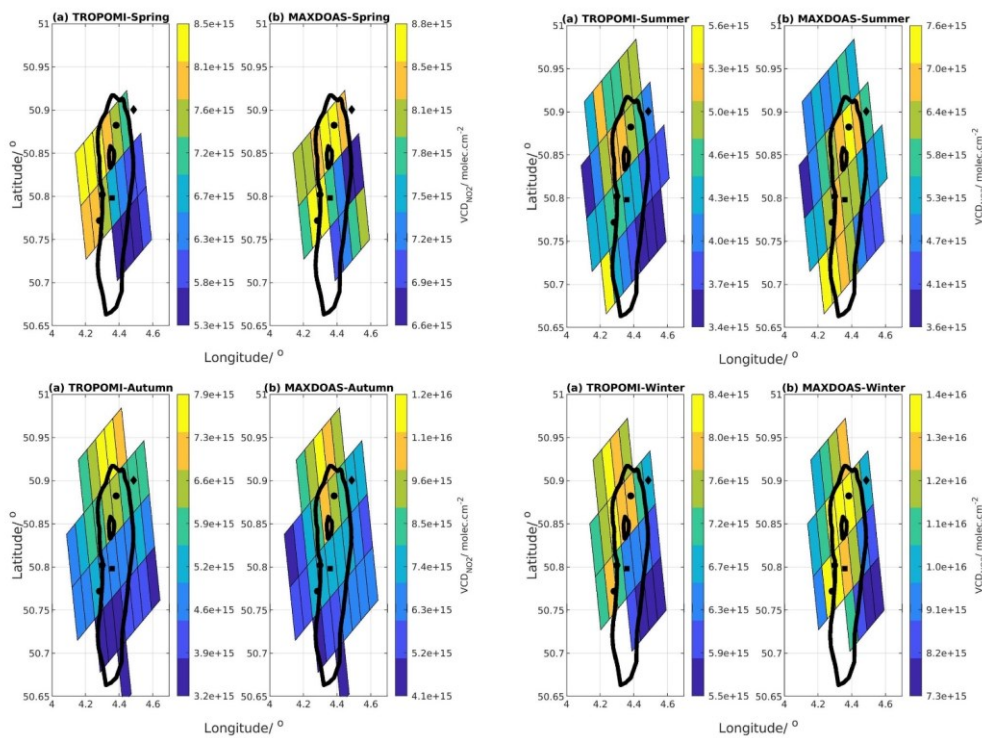
Formatted: Normal, No bullets or numbering

($R=0.70$), while lower correlations are reported in autumn, summer, and winter, with correlation coefficient values of 0.6067 , 0.5861 , and 0.5657 , respectively. It should be noted that during spring (2018 and 2019), the number of comparison points is smaller than for the other seasons, because TROPOMI data start from end of April 2018. During spring, the slope value is equal to 1.06088 , while during winter, summer, and autumn, the slope values are smaller (0.7867 , 0.5345 , and 0.7856 , respectively). Similar findings have been reported in several studies (Verhoelst et al., 2021; Tack et al., 2021; Judd et al., 2020; Dimitropoulou et al., 2020; Ialongo et al., 2019). When seasonally-averaged TROPOMI and MAX-DOAS pixels (the pixels shown in Fig. 21) are compared one-by-one (see seasonal (SEAS) in Fig. 23), both correlation coefficient (R in the range of 0.4262 - 0.9285) and slope values (s in the range of 0.4436 - 1.9084) improve considerably for spring and autumn.

In a second step, the impact of the spatial sampling is investigated. Generally, a varying number of MAX-DOAS NO_2 columns cover each TROPOMI pixel. The coverage percentage is estimated as the ratio of the covered area by MAX-DOAS (i.e., number of coincident MAX-DOAS NO_2 VCDs) inside each TROPOMI pixel to the total number of MAX-DOAS NO_2 VCDs that could fill in the TROPOMI pixel. When selecting only TROPOMI pixels covered by at least a given percentage of MAX-DOAS grids (10% and 20%), it is found that the correlation between both datasets improves for all seasons, except summer for a coverage equal and greater than 20%. The most significant improvement is observed during spring. The correlation coefficient value is equal to 0.82 (instead of 0.70) when taking into account TROPOMI pixels covered more than 20% by MAX-DOAS retrievals. Despite the better agreement in terms of correlation coefficient, TROPOMI columns are still 30% lower than MAX-DOAS measurements, in line with previously published studies.

The seasonal regression analysis parameters between TROPOMI and dual-scan MAX-DOAS measurements derived in the present study are compared to the same parameters presented in Dimitropoulou et al. (2020), see Table 4. Both studies make use of the dual-scan MAX-DOAS instrument in Uccle. In addition to the different approach (i.e., the retrieval of NO_2 horizontal profiles), in the present study, almost two years of measurements are used, while in Dimitropoulou et al. (2020), only one year is exploited for the TROPOMI validation. In Table 4, for the present study, only one year of measurements are used to have a comparable time coverage for both studies. As presented in Table 4, here, the largest slope value is found in spring, while winter, both in the present study and in Dimitropoulou et al. (2020), in winter. The season in which the highest correlation coefficient is obtained differs between both studies (here, in spring, in autumn in Dimitropoulou et al. (2020)). The main advantage of the new mapping MAX-DOAS technique is the larger number of comparison points between TROPOMI and MAX-DOAS leading to significantly more reliable statistics. In the present study, the deviation of the comparison points from the fitted regression line is increased mainly because of the uncertainties in the horizontal inversion approach. The scatter increase is reflected in the correlation coefficient values, which are smaller for all seasons, except spring and winter. Regarding the slope value, it is larger in spring and summer, and is smaller in autumn and winter during all seasons.

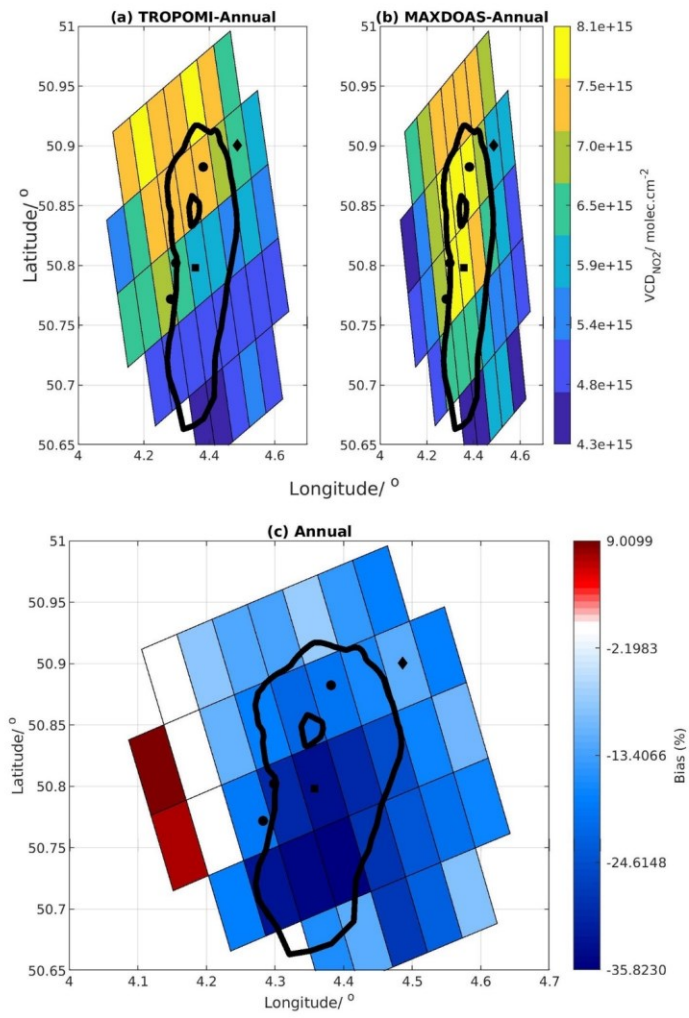




920

Figure 21. Seasonal tropospheric NO₂ VCD grids (TROPOMI grids) as retrieved over Brussels by the TROPOMI and MAX-DOAS instruments. The black square shows the MAX-DOAS position, the black polygon the National Airport, the black dots the NO₂ hotspots, and the black line represents the Brussels Ring motorway.

925



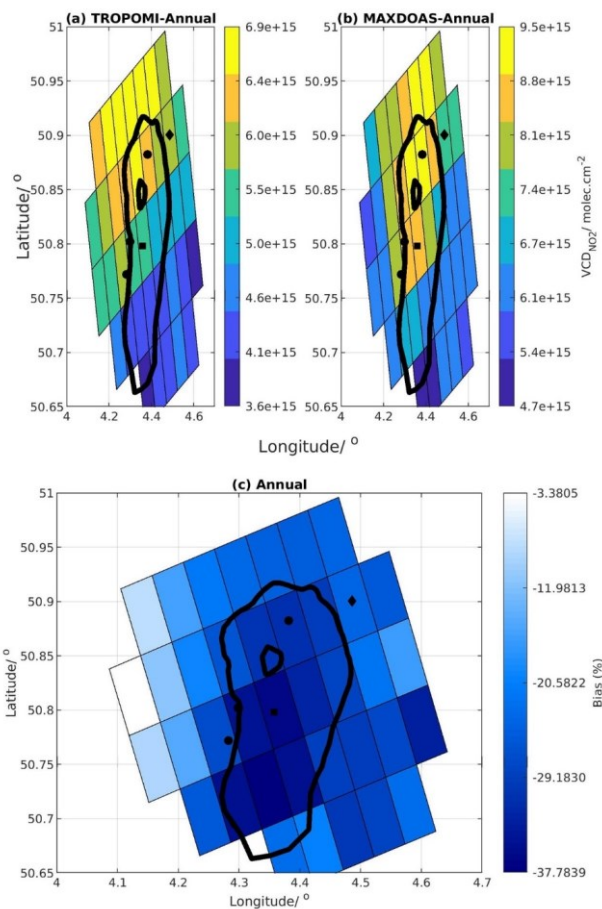


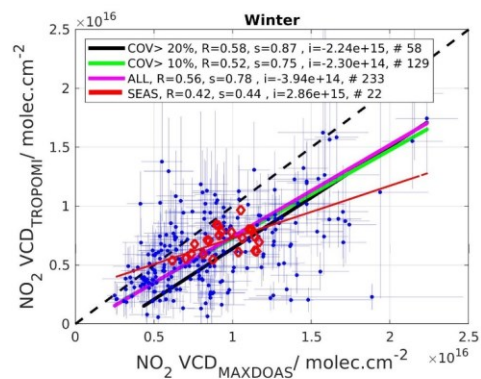
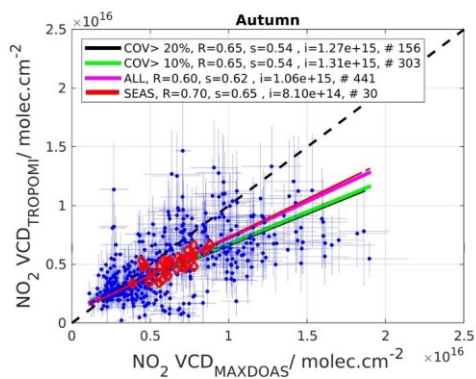
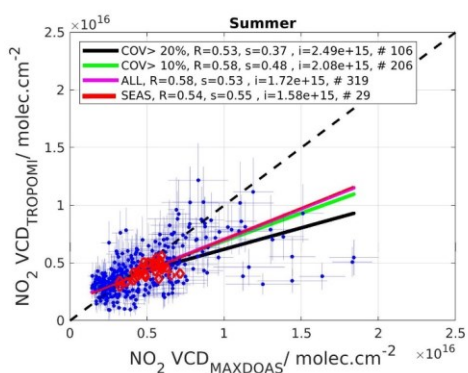
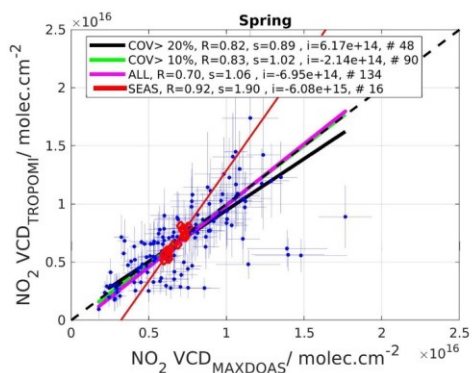
Figure 22. Annual (e.g., based over the two years of observations) tropospheric NO₂ VCD grids (TROPOMI grids) as retrieved over Brussels by the (a) TROPOMI and (b) MAX-DOAS instruments. (c) Annual bias between tropospheric NO₂ VCD as observed by TROPOMI and MAX-DOAS instruments (the negative values are shown with blue color, zero with white, and positive values with red). The black square shows the MAX-DOAS instrument location, the black polygon the National Airport, the black dots the NO₂ hotspots, and the black line represents the Brussels Ring road.

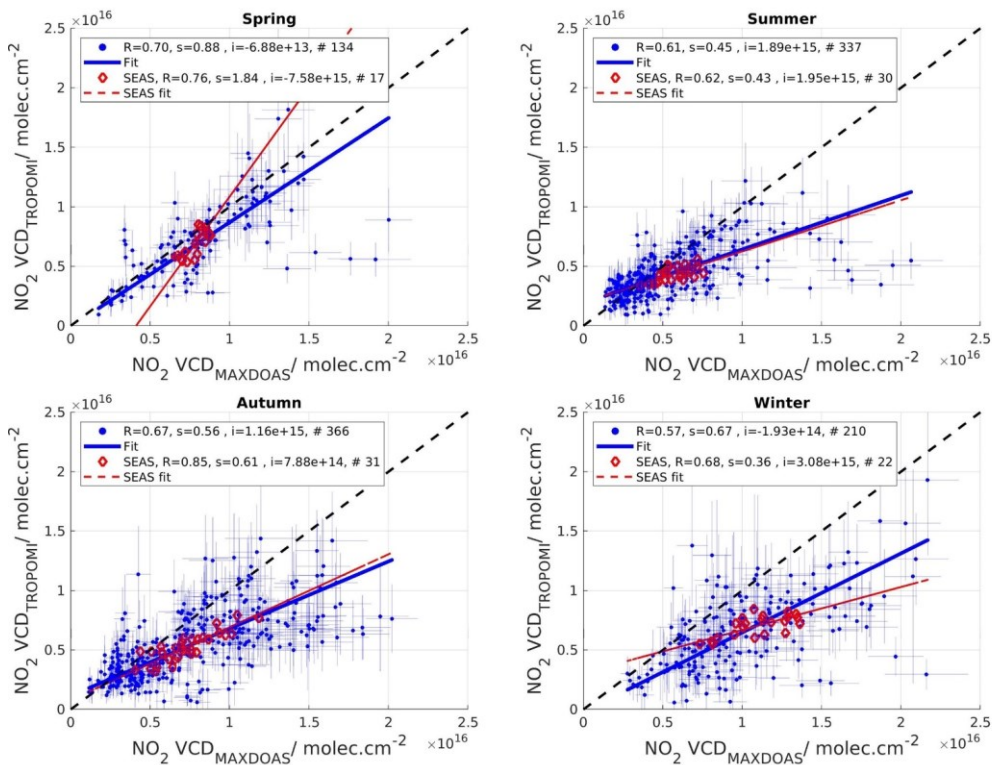
930

935

940

945





950

Figure 23. Seasonal scatter plots of tropospheric NO₂ columns derived from the dual-scan MAX-DOAS and TROPOMI measurements over Brussels. ~~Magenta~~Blue line: Regression analysis results when all the MAX-DOAS and TROPOMI pixels are included in the comparison. ~~Green and black lines:~~ Regression analysis results when TROPOMI pixels covered (i.e., COV) by more than 10 and 20 % of the horizontal profiles of MAX-DOAS NO₂ columns are included in the comparison. ~~Red line:~~ Seasonal average analysis generated by the pixels in Fig. 21.

955

960

965

Table 4. Summary of the regression analysis parameters (e.g., correlation coefficient (R) and slope (s) and the number of data points (N) derived in the present study during only one year of observations (i.e., number of pixels) and in Dimitropoulou et al. (2020). Please note that R (seasonal) and s (seasonal) corresponds to SEAS in Figure 23.

Season	Spring	Summer	Autumn	Winter
R	<u>0.6670</u>	<u>0.6065</u>	<u>0.5745</u>	<u>0.6267</u>
R (seasonal)	<u>0.9376</u>	<u>0.8862</u>	<u>0.46</u>	<u>0.75</u>
R (Dimitropoulou et al., 2020)	0.69	0.77	0.85	0.60
s	<u>0.9088</u>	<u>0.7664</u>	<u>0.5685</u>	<u>1.71</u>
s (seasonal)	<u>0.94</u>	<u>0.8743</u>	<u>0.73</u>	<u>0.6036</u>
s (Dimitropoulou et al., 2020)	<u>1.84</u>	0.58	<u>0.7462</u>	<u>0.70</u>
N	0.47	<u>247</u>	0.61	0.81
N (Dimitropoulou et al., 2020)	<u>139</u>	<u>252</u>	<u>106</u>	<u>92</u>
	<u>134</u>	58	<u>99</u>	<u>84</u>
	16		36	13

970

975

980

985

6.7 Conclusions

Two years (March 2018 to February 2020) of dual-scan MAX-DOAS measurements in Uccle (urban background site located in the south of the Brussels-Capital Region) were used to develop a new strategy for the retrieval of near-surface NO₂ concentrations and aerosol extinction horizontal profiles. A full dual-scan measurement is composed of one vertical scan at a fixed azimuthal direction pointing towards the city center and horizontal scans in ten azimuthal directions at a fixed low elevation angle (2°).

The first step of this new retrieval strategy is to analyze measured radiance spectra in six different fitting windows. This provides O₄ and NO₂ dSCDs at the following six wavelengths: 343 nm, 360 nm, 380 nm, 447 nm, 477 nm and 530 nm. Then, information about the vertical extent of NO₂ in the troposphere (MLH_{NO2}) is derived from profile retrievals in the main azimuthal direction performed using the OEM-based MMF algorithm. In the third step, a new parameterization technique is applied, with MLH_{NO2}, measured O₄ dSCDs, and measurement geometry being used as input parameters to retrieve the horizontal sensitivity of NO₂ and, consequently, the NO₂ near-surface concentrations and VCDs, near-surface aerosol extinction and AODs in all the azimuthal directions for the six different wavelengths. Compared to the method presented in Dimitropoulou et al., (2020), the new retrieval method offers the possibility of the direct determination of L_{NO2}, and near-surface aerosol extinction based on the measured O₄ dSCDs.

The retrieved dual-scan NO₂ near-surface concentrations and VCDs are verified via comparisons to the MMF NO₂ vertical profiles derived in the main azimuthal directions and in three additional azimuthal directions. A good overall agreement is found for the two comparisons during the two years of measurements.

The dependence of the horizontal sensitivity on the wavelength is then used to develop a new OEM-based horizontal distribution inversion approach. Considering a horizontal box model, horizontal NO₂ and aerosol extinction profiles are retrieved in an output horizontal grid of 500m thickness starting from the instrument to each of the measurement maximum horizontal representative distance.

The daily variability of NO₂ horizontal profiles in all the azimuthal directions provides information about the location of the NO₂ hotspots in the Brussels-Capital Region and how the plumes are transported. Similarly, the NO₂ horizontal profiles' seasonal variability over March 2018-February 2020 reveals that the NO₂ hotspots are mainly found above the Brussels city-center, the Drogenbos power plant and the NW part of the Ring road during all seasons.

On 28 June 2019, airborne measurements (APEX) of NO₂ were performed over Brussels. The MAX-DOAS NO₂ VCD horizontal profiles are compared to APEX, mobile car-DOAS (i.e., AEROMOBIL), and TROPOMI measurements, and a good overall agreement is found between the different data sets for this day.

In the last part of the study, MAX-DOAS retrievals are compared to TROPOMI tropospheric NO₂ observations over the March 2018- February 2020 period. The comparison of seasonal maps shows a good overall agreement between both datasets as to the NO₂ horizontal distribution over the Brussels area. ~~During all seasons, except summer, this agreement improves systematically when only TROPOMI pixels covered by a minimum of 20% of MAX-DOAS grid cells are compared, showing the benefit of ground-based measurements at high horizontal resolution for the validation of high-resolution space-borne air quality measurements.~~ Results also show that during all seasons, TROPOMI underestimates the MAX-DOAS tropospheric NO₂ columns.

Overall, our investigation about the spatial sampling lead to the following three important findings:

1. The dual-scan multi-wavelength approach allows a ~~better~~good identification of the main emissions sources in urban regions, in agreement with the spatial allocation of the main emission sources observed by APEX and TROPOMI.
2. ~~The~~ characterization of the NO₂ concentration horizontal field using the dual scan multi-wavelength approach results in obtaining ~~larger~~ slope values closer to unity between TROPOMI and MAX-DOAS observations. The high spatial resolution of TROPOMI requires ground-based measurement that can provide information about the horizontal distribution of tropospheric NO₂ columns in urban regions.
3. ~~Even for a better spatial sampling between TROPOMI and ground-based observations, TROPOMI still underestimates the ground-based measurements (see Fig. 22). Therefore, this is an additional indication that this underestimation is caused by other factors.~~
2. ~~The role of the a-priori NO₂ profile shape in the TROPOMI retrievals was investigated and TROPOMI tropospheric NO₂ columns are recalculated with the MAX-DOAS vertical profiles. We show that the knowledge of the NO₂ horizontal distribution derived by the MAX-DOAS measurements combined with a more adequate a-priori profile in TROPOMI retrievals leads to a much better agreement between satellite and ground-based data.~~

To conclude, our study presents a new horizontal distribution inversion approach for NO₂ and aerosols developed by using dual-scan multi-wavelength MAX-DOAS measurements over an urban area. This approach provides a better characterization of the horizontal distribution of an important urban pollutant, NO₂, which leads to an improved agreement between satellite and MAX-DOAS measurements in moderate to highly polluted conditions. Based on our study, further modifications of the measurement mode aiming at a better sampling of the vertical and horizontal NO₂ distribution could be implemented and investigated. For instance, performing vertical scans in several azimuthal directions throughout the day and/or horizontal scans in more than ten azimuthal directions could further improve our knowledge about the tropospheric NO₂ spatial variability in urban regions, and therefore the satellite validation results in those conditions.

Data availability. The datasets generated and analyzed in the present work are available from the corresponding author on request.

Formatted: List Paragraph, Numbered + Level: 1 + Numbering Style: 1, 2, 3, ... + Start at: 1 + Alignment: Left
Aligned at: 0,63 cm + Indent at: 1,27 cm

Formatted: Font color: Text 1

Author contributions. ED undertook the development and validation of the dual-scan multi-wavelength MAX-DOAS retrieval strategy in Uccle, exploited the MAX-DOAS retrievals during two year, performed the validation of the TROPOMI tropospheric NO₂ columns, and wrote the paper. FH supported and guided ED in the development of the dual-scan multi-wavelength MAX-DOAS retrieval strategy, provided general guidelines, and revised and edited the paper. MMF provided the MMF inversion algorithm and the RTM as well as supporting and guiding ED in the new OEM-based horizontal profile retrieval. FT provided the airborne APEX dataset and contributed to scientific discussions. GP provided the dataset of the TROPOMI tropospheric NO₂ columns and supported ED in the TROPOMI validation approaches. AM provided the AEROMOBIL dataset and contributed to scientific discussions. CF and CH provided technical and software support for the MAX-DOAS instrument in Uccle. CF developed the QDOAS software and guided ED in the DOAS analysis. FF provided the RIO model dataset. MVR supervised the present work, provided general guidelines and valuable comments during the whole process of the paper preparation, and revised and edited the paper. All authors reviewed, discussed and commented on the paper.

Competing interests. I declare that I or my co-authors have competing interests as follows: Michel Van Roozendael is associate editor of AMT.

References

- Aliwell, S.R., Van Roozendael, M., Johnston, P.V., Richter, A., Wagner, T., Arlander, D.W., Burrows, J.P., Fish, D.J., Jones, R.L., Tørnkqvist, K.K. and Lambert, J.C., 2002. Analysis for BrO in zenith-sky spectra: An intercomparison exercise for analysis improvement. *Journal of Geophysical Research: Atmospheres*, 107(D14), pp.ACH-10.
- Barret, B., De Maziere, M., and Demoulin, P.: Retrieval and characterisation of ozone profiles from solar infrared spectra at the Jungfraujoch, *J. Geophys. Res.*, 107 (D24), 4788, doi:10.1029/2001JD001298, 2002.
- Beirle, S., Dörner, S., Donner, S., Remmers, J., Wang, Y., and Wagner, T.: The Mainz profile algorithm (MAPA), *Atmos. Meas. Tech.*, 12, 1785–1806, <https://doi.org/10.5194/amt-12-1785-2019>, 2019.
- Beirle, S., Platt, U., Wenig, M., and Wagner, T.: Weekly cycle of NO₂ by GOME measurements: a signature of anthropogenic sources, *Atmos. Chem. Phys.*, 3, 2225–2232, <https://doi.org/10.5194/acp-3-2225-2003>, 2003.
- Bösch, T., Rozanov, V., Richter, A., Peters, E., Rozanov, A., Wittrock, F., Merlaud, A., Lampel, J., Schmitt, S., de Haij, M., Berkhout, S., Henzing, B., Apituley, A., den Hoed, M., Vonk, J., Tiefengraber, M., Müller, M., and Burrows, J. P.: BOREAS – a new MAX-DOAS profile retrieval algorithm for aerosols and trace gases, *Atmos. Meas. Tech.*, 11, 6833–

6859, <https://doi.org/10.5194/amt-11-6833-2018>, 2018.

1090 Burrows, J. P., Weber, M., Buchwitz, M., Rosanov, V. V., Ladstatter, A., Weissenmayer, A., Richter, A., DeBeek, R., Hoogen, R., Bramstedt, K., and Eichmann, K. U.: The Global Ozone Monitoring Experiment (GOME): Mission concept and first scientific results, *J. Atmos. Sci.*, 56, 151–175, 1999.

Chance, K. V. and Spurr, R. J. D.: Ring effect studies: Rayleigh scattering, including molecular parameters for rotational Raman scattering, and the Fraunhofer spectrum, *Appl. Optics*, 36, 5224–5230, doi:10.1364/AO.36.005224, 1997.

1095 Chan, K. L., Wiegner, M., van Geffen, J., De Smedt, I., Alberti, C., Cheng, Z., Ye, S., and Wenig, M.: MAX-DOAS measurements of tropospheric NO₂ and HCHO in Munich and the comparison to OMI and TROPOMI satellite observations, *Atmos. Meas. Tech.*, 13, 4499–4520, <https://doi.org/10.5194/amt-13-4499-2020>, 2020.

Chen, T. M., Kuschner, W. G., Gokhale, J., & Shofer, S. (2007). Outdoor air pollution: nitrogen dioxide, sulfur dioxide, and carbon monoxide health effects. *The American journal of the medical sciences*, 333(4), 249-256.

1100 Clémer, K., Van Roozendaal, M., Fayt, C., Hendrick, F., Hermans, C., Pinardi, G., Spurr, R., Wang, P., and De Mazière, M.: Multiple wavelength retrieval of tropospheric aerosol optical properties from MAXDOAS measurements in Beijing, *Atmos. Meas. Tech.*, 3, 863–878, <https://doi.org/10.5194/amt-3-863-2010>, 2010.

Compernelle, S., Argyrouli, A., Lutz, R., Sneep, M., Lambert, J.-C., Fjæraa, A. M., Hubert, D., Keppens, A., Loyola, D., O'Connor, E., Romahn, F., Stammes, P., Verhoelst, T., and Wang, P.: Validation of the Sentinel-5 Precursor TROPOMI cloud data with Cloudnet, Aura OMI O₂–O₂, MODIS, and Suomi-NPP VIIRS, *Atmos. Meas. Tech.*, 14, 2451–2476, <https://doi.org/10.5194/amt-14-2451-2021>, 2021.

Dimitropoulou, E., Hendrick, F., Pinardi, G., Friedrich, M. M., Merlaud, A., Tack, F., De Longueville, H., Fayt, C., Hermans, C., Laffineur, Q., Fierens, F., and Van Roozendaal, M.: Validation of TROPOMI tropospheric NO₂ columns using dual scan multi-axis differential optical absorption spectroscopy (MAX-DOAS) measurements in Uccle, Brussels, *Atmos. Meas. Tech.*, 13, 5165–5191, <https://doi.org/10.5194/amt-13-5165-2020>, 2020.

Douros, J., Eskes, H., van Geffen, J., Boersma, F., Compernelle, S., Pinardi, G., Blechschmidt, A.-M., Peuch, V.-H., Colette, A., and Veeffkind P.: Comparing Sentinel-5P TROPOMI NO₂ column observations with the CAMS-regional air quality ensemble, in preparation.

Eskes, H.J. and Eichmann, K.U.: *S5P MPC Product Readme Nitrogen Dioxide*. Report S5P-MPC-KNMI PRF-NO₂, version 1.4, 6 August 2019, ESA, available at: <http://www.tropomi.eu/documents/prf/>, 17 March, 2020.

1115 Fayt, C., De Smedt, I., Letocart, V., Merlaud, A., Pinardi, G., and Van Roozendaal, M.: QDOAS Software user manual, <http://uv-vis.aeronomie.be/software/QDOAS/index.php>, 2011.

[Finkenzeller, H., & Volkamer, R.: O₂–2 CIA in the gas phase: Cross-section of weak bands, and continuum absorption between 297–500 nm. *Journal of Quantitative Spectroscopy and Radiative Transfer*, 108063, 2022.](#)

1120 Fleischmann, O. C., Hartmann, M., Burrows, J. P., and Orphal, J.: New ultraviolet absorption cross-sections of BrO at atmospheric temperatures measured by time-windowing Fourier transform spectroscopy, *J. Photoch. Photobio. A*, 168, 117–132, 2004.

Formatted: Font color: Text 1

Formatted: French (Belgium)

- Friedrich, M. M., Rivera, C., Stremme, W., Ojeda, Z., Arellano, J., Bezanilla, A., García-Reynoso, J. A., and Grutter, M.: NO₂ vertical profiles and column densities from MAX-DOAS measurements in Mexico City, *Atmos. Meas. Tech.*, 12, 2545–2565, <https://doi.org/10.5194/amt-12-2545-2019>, 2019.
- 1125 Hendrick, F., Müller, J.-F., Clémer, K., Wang, P., De Mazière, M., Fayt, C., Gielen, C., Hermans, C., Ma, J. Z., Pinardi, G., Stavroukou, T., Vlemmix, T., and Van Roozendael, M.: Four years of ground-based MAX-DOAS observations of HONO and NO₂ in the Beijing area, *Atmos. Chem. Phys.*, 14, 765–781, <https://doi.org/10.5194/acp-14-765-2014>, 2014.
- Hönninger, G., von Friedeburg, C., and Platt, U.: Multi axis differential optical absorption spectroscopy (MAX-DOAS), *Atmos. Chem. Phys.*, 4, 231–254, doi:10.5194/acp-4-231-2004, 2004.
- 1130 Hooyberghs, J., Mensink, C., Dumont, G. and Fierens, F., 2006. Spatial interpolation of ambient ozone concentrations from sparse monitoring points in Belgium. *Journal of Environmental Monitoring*, 8(11), pp.1129-1135.
- Ialongo, I., Virta, H., Eskes, H., Hovila, J., and Douros, J.: Comparison of TROPOMI/Sentinel 5 Precursor NO₂ observations with ground-based measurements in Helsinki, *Atmos. Meas. Tech. Discuss.*, <https://doi.org/10.5194/amt-2019-329>, in review, 2019.
- 1135 Irie, H., Takashima, H., Kanaya, Y., Boersma, K. F., Gast, L., Wittrock, F., Brunner, D., Zhou, Y., and Van Roozendael, M.: Eight-component retrievals from ground-based MAXDOAS observations, *Atmos. Meas. Tech.*, 4, 1027–1044, <https://doi.org/10.5194/amt-4-1027-2011>, 2011.
- Irie, H., Boersma, K. F., Kanaya, Y., Takashima, H., Pan, X., and Wang, Z. F.: Quantitative bias estimates for tropospheric NO₂ columns retrieved from SCIAMACHY, OMI, and GOME-2 using a common standard for East Asia, *Atmos. Meas. Tech.*, 5, 2403–2411, <https://doi.org/10.5194/amt-5-2403-2012>, 2012.
- 1140 Janssen, S., Dumont, G., Fierens, F. and Mensink, C., 2008. Spatial interpolation of air pollution measurements using CORINE land cover data. *Atmospheric Environment*, 42(20), pp.4884-4903.
- Judd, L. M., Al-Saadi, J. A., Szykman, J. J., Valin, L. C., Janz, S. J., Kowalewski, M. G., Eskes, H. J., Veeckind, J. P., Cede, A., Mueller, M., Gebetsberger, M., Swap, R., Pierce, R. B., Nowlan, C. R., Abad, G. G., Nehrir, A., and Williams, D.: Evaluating Sentinel-5P TROPOMI tropospheric NO₂ column densities with airborne and Pandora spectrometers near New York City and Long Island Sound, *Atmos. Meas. Tech.*, 13, 6113–6140, <https://doi.org/10.5194/amt-13-6113-2020>, 2020.
- 1145 Khomenko, S., Cirach, M., Pereira-Barboza, E., Mueller, N., Barrera-Gómez, J., Rojas-Rueda, D., de Hoogh, K., Hoek, G. and Nieuwenhuijsen, M., 2021. Premature mortality due to air pollution in European cities: a health impact assessment. *The Lancet Planetary Health*, 5(3), pp.e121-e134.
- Klimont, Z., Kupiainen, K., Heyes, C., Purohit, P., Cofala, J., Rafaj, P., Borken-Kleefeld, J., and Schöpp, W.: Global anthropogenic emissions of particulate matter including black carbon, *Atmos. Chem. Phys.*, 17, 8681–8723, <https://doi.org/10.5194/acp-17-8681-2017>, 2017.
- 1155 Kreher, K., Van Roozendael, M., Hendrick, F., Apituley, A., Dimitropoulou, E., Frieß, U., Richter, A., Wagner, T., Abuhassan, N., Ang, L., Anguas, M., Bais, A., Benavent, N., Bösch, T., Bognar, K., Borovski, A., Bruchkouski, I., Cede, A., Chan,

- K. L., Donner, S., Drosoglou, T., Fayt, C., Finkenzeller, H., Garcia-Nieto, D., Gielen, C., Gómez-Martín, L., Hao, N., Herman, J. R., Hermans, C., Hoque, S., Irie, H., Jin, J., Johnston, P., Khayyam Butt, J., Khokhar, F., Koenig, T. K., Kuhn, J., Kumar, V., Lampel, J., Liu, C., Ma, J., Merlaud, A., Mishra, A. K., Müller, M., Navarro-Comas, M., Ostendorf, M., Pazmino, A., Peters, E., Pinardi, G., Pinharanda, M., Piters, A., Platt, U., Postlyakov, O., Prados-Roman, C., Puentedura, O., Quereil, R., Saiz-Lopez, A., Schönhardt, A., Schreier, S. F., Seyler, A., Sinha, V., Spinci, E., Strong, K., Tack, F., Tian, X., Tiefengraber, M., Tirpitz, J.-L., van Gent, J., Volkamer, R., Vrekoussis, M., Wang, S., Wang, Z., Wenig, M., Wittrock, F., Xie, P. H., Xu, J., Yela, M., Zhang, C., and Zhao, X.: Intercomparison of NO₂, O₄, O₃ and HCHO slant column measurements by MAX-DOAS and zenith-sky UV-Visible spectrometers during the CINDI-2 campaign, *Atmos. Meas. Tech. Discuss.*, <https://doi.org/10.5194/amt-2019-157>, in review, 2019.
- 1160 Kurucz, R.L., Furenlid, I., Brault, J., and Testerman, L.: Solar flux atlas from 296 to 1300 nm, National Solar Observatory, Sunspot, New Mexico, U.S.A., 1984.
- Meller, R. and Moortgat, G. K.: Temperature dependence of the absorption cross sections of formaldehyde between 223 and 323K in the wavelength range 225–375nm, *J. Geophys. Res.*, 105, 7089–7101, 2000.
- 1170 Merlaud, A., Van Roozendael, M., Theys, N., Fayt, C., Hermans, C., Quennehen, B., Schwarzenboeck, A., Ancellet, G., Pommier, M., Pelon, J., Burkhardt, J., Stohl, A., and De Mazière, M.: Airborne DOAS measurements in Arctic: vertical distributions of aerosol extinction coefficient and NO₂ concentration, *Atmos. Chem. Phys.*, 11, 9219–9236, <https://doi.org/10.5194/acp11-9219-2011>, 2011.
- Merlaud, A.: Development and use of compact instruments for tropospheric investigations based on optical spectroscopy from mobile platforms, Presses Universitaires de Louvain, 2013.
- 1175 Pinardi, G., Hendrick, F., Clémer, K., Lambert, J. C., Bai, J., and Van Roozendael, M.: On the use of the MAX-DOAS technique for the validation of tropospheric NO₂ column measurements from satellite, *Proc. Eumetsat Conf.*, ISBN 978-92-9110-082-8, 2008.
- Puķite, J., Kühl, S., Deutschmann, T., Platt, U., and Wagner, T.: Extending differential optical absorption spectroscopy for limb measurements in the UV, *Atmos. Meas. Tech.*, 3, 631–653, <https://doi.org/10.5194/amt-3-631-2010>, 2010.
- 1180 Quaas, Johannes, Olivier Boucher, Nicolas Bellouin, and Stefan Kinne. "Satellite-based estimate of the direct and indirect aerosol climate forcing." *Journal of Geophysical Research: Atmospheres* 113, no. D5 (2008).
- Rodgers, C. D.: Inverse Methods for Atmospheric Sounding, Theory and Practice, World Scientific Publishing, Singapore – New Jersey – London – Hong Kong, 2000.
- 1185 Rothman, L.S., Gordon, I.E., Babikov, Y., Barbe, A., Benner, D.C., Bernath, P.F., Birk, M., Bizzocchi, L., Boudon, V., Brown, L.R. and Campargue, A., 2013. The HITRAN2012 molecular spectroscopic database. *Journal of Quantitative Spectroscopy and Radiative Transfer*, 130, pp.4-50. Seinfeld, J. H. and Pandis, S. N.: Atmospheric Chemistry and Physics: From Air Pollution to Climate Change, John Wiley & Sons, Inc., 1998.
- 1190 Schreier, S. F., Bösch, T., Richter, A., Lange, K., Revesz, M., Weihs, P., Vrekoussis, M., and Lotteraner, C.: Evaluation of UV-visible MAX-DOAS aerosol profiling products by comparison with ceilometer, sun photometer, and in situ

- observations in Vienna, Austria, *Atmos. Meas. Tech.*, 14, 5299–5318, <https://doi.org/10.5194/amt-14-5299-2021>, 2021.
- Serdychenko, A., Gorshelev, V., Weber, M., Chehade, W., and Burrows, J. P.: High spectral resolution ozone absorption crosssections – Part 2: Temperature dependence, *Atmos. Meas. Tech.*, 7, 625–636, doi:10.5194/amt-7-625-2014, 2014.
- 1195 Sinreich, R., Volkamer, R., Filsinger, F., Frieß, U., Kern, C., Platt, U., Sebastián, O., and Wagner, T.: MAX-DOAS detection of glyoxal during ICARTT 2004, *Atmos. Chem. Phys.*, 7, 1293–1303, <https://doi.org/10.5194/acp-7-1293-2007>, 2007.
- Sinreich, R., Merten, A., Molina, L., and Volkamer, R.: Parameterizing radiative transfer to convert MAX-DOAS dSCDs into near-surface box-averaged mixing ratios, *Atmos. Meas. Tech.*, 6, 1521–1532, doi:10.5194/amt-6-1521-2013, 2013.
- Spurr, R. J.: VLIDORT: A linearized pseudo-spherical vector discrete ordinate radiative transfer code for forward model and retrieval studies in multilayer multiple scattering media, *J. Quant. Spectrosc. Ra.*, 102, 316–342, 2006.
- 1200 Tack, F., Merlaud, A., Iordache, M.-D., Danckaert, T., Yu, H., Fayt, C., Meuleman, K., Deutsch, F., Fierens, F., and Van Roozendael, M.: High-resolution mapping of the NO₂ spatial distribution over Belgian urban areas based on airborne APEX remote sensing, *Atmos. Meas. Tech.*, 10, 1665–1688, <https://doi.org/10.5194/amt-10-1665-2017>, 2017.
- Tack, F., Merlaud, A., Meier, A. C., Vlemmix, T., Ruhtz, T., Iordache, M.-D., Ge, X., van der Wal, L., Schuettemeyer, D., Ardelean, M., Calcan, A., Constantin, D., Schönhardt, A., Meuleman, K., Richter, A., and Van Roozendael, M.:
1205 Intercomparison of four airborne imaging DOAS systems for tropospheric NO₂ mapping – the AROMAPEX campaign, *Atmos. Meas. Tech.*, 12, 211–236, <https://doi.org/10.5194/amt-12-211-2019>, 2019.
- Tack, F., Merlaud, A., Iordache, M.-D., Pinardi, G., Dimitropoulou, E., Eskes, H., Bomans, B., Veefkind, P., and Van Roozendael, M.: Assessment of the TROPOMI tropospheric NO₂ product based on airborne APEX observations, *Atmos. Meas. Tech.*, 14, 615–646, <https://doi.org/10.5194/amt-14-615-2021>, 2021.
- 1210 Thalman, R. and Volkamer, R.: Temperature dependent absorption cross-sections of O₂-O₂ collision pairs between 340 and 630nm and at atmospherically relevant pressure, *Phys. Chem. Chem. Phys.*, 15, 15371–15381, doi:10.1039/C3CP50968K, 2013.
- Tirpitz, J.-L., Frieß, U., Hendrick, F., Alberti, C., Allaart, M., Apituley, A., Bais, A., Beirle, S., Berkhout, S., Bognar, K., Bösch, T., Bruchkouski, I., Cede, A., Chan, K. L., den Hoed, M., Donner, S., Drosoglou, T., Fayt, C., Friedrich, M. M.,
1215 Frumau, A., Gast, L., Gielen, C., Gomez-Martín, L., Hao, N., Hensen, A., Henzing, B., Hermans, C., Jin, J., Kreher, K., Kuhn, J., Lampel, J., Li, A., Liu, C., Liu, H., Ma, J., Merlaud, A., Peters, E., Pinardi, G., Piders, A., Platt, U., Puentedura, O., Richter, A., Schmitt, S., Spinei, E., Stein Zweers, D., Strong, K., Swart, D., Tack, F., Tiefengraber, M., van der Hoff, R., van Roozendael, M., Vlemmix, T., Vonk, J., Wagner, T., Wang, Y., Wang, Z., Wenig, M., Wiegner, M., Wittrock, F., Xie, P., Xing, C., Xu, J., Yela, M., Zhang, C., and Zhao, X.: Intercomparison of MAX-DOAS vertical profile retrieval algorithms: studies on field data from the CINDI-2 campaign, *Atmos. Meas. Tech.*, 14, 1–35, <https://doi.org/10.5194/amt-14-1-2021>, 2021.
- 1220 van Geffen, J. H. G. M., Eskes, H. J., Boersma, K. F. and Veefkind, J. P.: TROPOMI ATBD of the total and tropospheric NO₂ data products, Report S5P-KNMI-L2-0005-RP, version 2.2.0, released 16 June 2021, KNMI, De Bilt, The Netherlands, <http://www.tropomi.eu/data-products/nitrogen-dioxide/>, 2021a.

- 1225 van Geffen, J., Eskes, H., Compernelle, S., Pinardi, G., Verhoelst, T., Lambert, J.-C., Sneep, M., ter Linden, M., Ludewig, A.,
Boersma, K. F., and Veefkind, J. P.: Sentinel-5P TROPOMI NO₂ retrieval: impact of version v2.2 improvements and
comparisons with OMI and ground-based data, *Atmos. Meas. Tech. Discuss.* [preprint], [https://doi.org/10.5194/amt-](https://doi.org/10.5194/amt-2021-329)
2021-329, in review, 2021b. Vandaele, A., Hermans, C., Simon, P., Carleer, M., Colin, R., Fally, S., Mérienne, M.,
Jenouvrier, A., and Coquart, B.: Measurements of the NO₂ absorption cross-section from 42000cm⁻¹ to 10000cm⁻¹
1230 (238–1000nm) at 220K and 294K, *J. Quant. Spectrosc. Ra.*, 59, 171–184, 1998.
- Veefkind, J. P., Boersma, K. F., Wang, J., Kurosu, T. P., Krotkov, N., Chance, K., and Levelt, P. F.: Global satellite analysis
of the relation between aerosols and short-lived trace gases, *Atmos. Chem. Phys.*, 11, 1255–1267, doi:10.5194/acp-11-
1255-2011, 2011.
- Verhoelst, T., Compernelle, S., Pinardi, G., Lambert, J.-C., Eskes, H. J., Eichmann, K.-U., Fjæraa, A. M., Granville, J.,
1235 Niemeijer, S., Cede, A., Tiefengraber, M., Hendrick, F., Pazmiño, A., Bais, A., Bazureau, A., Boersma, K. F., Bogner,
K., Dehn, A., Donner, S., Elokho, A., Gebetsberger, M., Goutail, F., Grutter de la Mora, M., Gruzdev, A., Gratsea, M.,
Hansen, G. H., Irie, H., Jepsen, N., Kanaya, Y., Karagiozidis, D., Kivi, R., Kreher, K., Levelt, P. F., Liu, C., Müller,
M., Navarro Comas, M., Piters, A. J. M., Pommereau, J.-P., Portafaix, T., Prados-Roman, C., Puentedura, O., Querel,
R., Remmers, J., Richter, A., Rimmer, J., Rivera Cárdenas, C., Saavedra de Miguel, L., Sinyakov, V. P., Stremme, W.,
1240 Strong, K., Van Roozendaal, M., Veefkind, J. P., Wagner, T., Wittrock, F., Yela González, M., and Zehner, C.: Ground-
based validation of the Copernicus Sentinel-5P TROPOMI NO₂ measurements with the NDACC ZSL-DOAS, MAX-
DOAS and Pandonia global networks, *Atmos. Meas. Tech.*, 14, 481–510, <https://doi.org/10.5194/amt-14-481-2021>,
2021.
- Vigouroux, C., Hendrick, F., Stavrakou, T., Dils, B., De Smedt, I., Hermans, C., Merlaud, A., Scolas, F., Senten, C.,
1245 Vanhaelewyn, G., Fally, S., Carleer, M., Metzger, J.-M., Müller, J.-F., Van Roozendaal, M., and De Mazière, M.:
Ground-based FTIR and MAX-DOAS observations of formaldehyde at Réunion Island and comparisons with satellite
and model data, *Atmos. Chem. Phys.*, 9, 9523–9544, <https://doi.org/10.5194/acp-9-9523-2009>, 2009.
- Wagner, T., Deutschmann, T., and Platt, U.: Determination of aerosol properties from MAX-DOAS observations of the Ring
effect, *Atmos. Meas. Tech.*, 2, 495–512, <https://doi.org/10.5194/amt-2-495-2009>, 2009.
- 1250 Wagner, T., Beirle, S., Brauers, T., Deutschmann, T., Frieß, U., Hak, C., Halla, J. D., Heue, K. P., Junkermann, W., Li, X.,
Platt, U., and Pundt-Gruber, I.: Inversion of tropospheric profiles of aerosol extinction and HCHO and NO₂ mixing
ratios from MAX-DOAS observations in Milano during the summer of 2003 and comparison with independent data sets,
Atmos. Meas. Tech., 4, 2685–2715, <https://doi.org/10.5194/amt-4-2685-2011>, 2011.
- Wagner, T., Beirle, S., Benavent, N., Bösch, T., Chan, K. L., Donner, S., Dörner, S., Fayt, C., Frieß, U., García-Nieto, D.,
1255 Gielen, C., González-Bartolome, D., Gomez, L., Hendrick, F., Henzing, B., Jin, J. L., Lampel, J., Ma, J., Mies, K.,
Navarro, M., Peters, E., Pinardi, G., Puentedura, O., Puķīte, J., Remmers, J., Richter, A., Saiz-Lopez, A., Shaiganfar, R.,
Sihler, H., Van Roozendaal, M., Wang, Y., and Yela, M.: Is a scaling factor required to obtain closure between measured
and modelled atmospheric O₄ absorptions? An assessment of uncertainties of measurements and radiative transfer

- simulations for 2 selected days during the MAD-CAT campaign, *Atmos. Meas. Tech.*, 12, 2745–2817, <https://doi.org/10.5194/amt-12-2745-2019>, 2019.
- 1260 Wang, Y., Li, A., Xie, P. H., Wagner, T., Chen, H., Liu, W. Q., and Liu, J. G.: A rapid method to derive horizontal distributions of trace gases and aerosols near the surface using multi-axis differential optical absorption spectroscopy, *Atmos. Meas. Tech.*, 7, 1663–1680, <https://doi.org/10.5194/amt-7-1663-2014>, 2014.
- 1265 Wang, Y., Pukite, J., Wagner, T., Donner, S., Beirle, S., Hilboll, A., Vrekoussis, M., Richter, A., Apituley, A., PETERS, A., Allaart, M., Eskes, H., Frumau, A., Roozendaal, M. V., Lampel, J., Platt, U., Schmitt, S., Swart, D., and Vonk, J.: Vertical Profiles of Tropospheric Ozone From MAX-DOAS Measurements During the CINDI-2 Campaign: Part 1 – Development of a New Retrieval Algorithm, *J. Geophys. Res.-Atmos.*, 123, 10637–10670, <https://doi.org/10.1029/2018JD028647>, 2018.
- 1270 Williams, J.E., Boersma, K.F., LeSager, P., and Verstraeten, W.W.: The high-resolution version of TM5-MP for optimized satellite retrievals: description and validation, *Geosci. Model Dev.*, 10, 721–750, <https://doi.org/10.5194/gmd-10-721-2017>, 2017.
- 1275 Wittrock, F., Oetjen, H., Richter, A., Fietkau, S., Medeke, T., Rozanov, A., and Burrows, J. P.: MAX-DOAS measurements of atmospheric trace gases in Ny-Ålesund - Radiative transfer studies and their application, *Atmos. Chem. Phys.*, 4, 955–966, <https://doi.org/10.5194/acp-4-955-2004>, 2004.

1280

1285

1290